

INVESTIGATION OF ASYMMETRIC HYBRID SUPERCAPACITOR BASED ON  
MORPHOLOGY OF ZINC OXIDE ELECTRODE MATERIALS FOR HIGH ENERGY  
SUPERCAPACITORS

by

SUMAIYAH NAJIB

A thesis submitted to Faculty of Engineering for Natural Sciences and Engineering in  
partial fulfillment of the requirements for the degree of Master of Science

SABANCI UNIVERSITY

AUGUST, 2020



INVESTIGATION OF ASYMMETRIC HYBRID SUPERCAPACITOR  
BASED ON MORPHOLOGY OF ZINC OXIDE ELECTRODE MATERIALS  
FOR HIGH ENERGY SUPERCAPACITORS

APPROVED BY:

Assoc. Prof. Dr. Emre Erdem .....  
(Thesis Supervisor)

Assoc. Prof. Dr. Meltem Sezen .....

Prof. Dr. Ebru Menşur Alkoy .....

DATE OF APPROVAL: 11/08/2020

© Sumaiyah Najib 2020

All Rights Reserved

## ABSTRACT

### INVESTIGATION OF ASYMMETRIC HYBRID SUPERCAPACITOR BASED ON MORPHOLOGY OF ZINC OXIDE ELECTRODE MATERIALS FOR HIGH ENERGY SUPERCAPACITORS

Sumaiyah Najib

Supervisor: Assoc.Prof.Dr. Emre Erdem

**Keywords:** nanomorphology, asymmetric hybrid supercapacitors, point defect, EPR spectroscopy

Supercapacitors are highly attractive for large number of emerging mobile devices for energy storage and harvesting issues. In this thesis, we present a summary of the recent developments in supercapacitor research and technology, including all kinds of supercapacitor design techniques using various electrode materials and production methods. It also covers the current progress achieved in novel materials for supercapacitor electrodes. The latest produced EDLC, Hybrid, Pseudo supercapacitors have also been described. Metal oxides, specifically ZnO, used as electrode materials with different morphologies are in focus here. The ZnO nanostructures were synthesized in the form of nanoparticles, nanoflowers and nanourchins. Structural, electronic and optical characterization of the samples were done via standard techniques such as XRD, SEM, Photoluminescence, Raman and UV-Vis spectroscopy. The point defect structures which are specific to each morphology has been investigated in terms of their concentration and location via state of art EPR spectroscopy. According to core-shell model the samples all revealed core defects however the defects on the surface smeared out. Finally, all three morphology has been tested as electrode material in a real supercapacitor device and the performance of the device, particularly the specific capacitance and the storage mechanism has been mediated by the point defects. Morphology dependent defective ZnO electrode enable to monitor the working principle of supercapacitor device from EDLC to pseudosupercapacitor.

## ÖZET

### YÜKSEK ENERJİ SÜPERKAPASİTÖRLERİ İÇİN ÇİNKO OKSİT ELEKTROT MALZEMELERİNİN MORFOLOJİSİNE DAYALI ASİMETRİK HİBRİD SÜPER KAPASİTÖRLERİN ARAŞTIRILMASI

Sumaiyah Najib

Danışman: Assoc.Prof.Dr. Emre Erdem

Anahtar Kelimeler: nanomorfoloji, asimetrik hibrit süperkapasitörler, nokta kusur, EPR spektroskopisi

Süper kapasitörler, enerji depolama ve hasat sorunları için çok sayıda yeni ortaya çıkan mobil cihaz için oldukça caziptir. Bu tezde, çeşitli elektrot malzemeleri ve üretim yöntemleri kullanarak her türlü süperkapasitör tasarım teknikleri dahil olmak üzere süperkapasitör araştırma ve teknolojisindeki son gelişmelerin bir özetini sunuyoruz. Aynı zamanda, süperkapasitör elektrotları için yeni materyallerde elde edilen mevcut ilerlemeyi de kapsamaktadır. En son üretilen EDLC, Hybrid, Pseudosüperkapasitörler de burada açıklanmıştır. Farklı morfolojilere sahip elektrot malzemeleri olarak kullanılan metal oksitler, özellikle ZnO, burada odaklanmaktadır. ZnO nanoyapıları, nanopartiküller, nanoflowerler ve nanourchinler şeklinde sentezlendi. Numunelerin yapısal, elektronik ve optik karakterizasyonu XRD, SEM, fotoluminesans, Raman ve UV-Vis spektroskopisi gibi standart tekniklerle yapılmıştır. Her bir morfolojiye özgü nokta kusur yapıları, konsantrasyonları ve konumları açısından EPR spektroskopisi ile araştırılmıştır. Core-shell modeline göre, numunelerin tümü çekirdek kusurlarını ortaya çıkarmış, ancak yüzeydeki kusurlar lekelenmiştir. Son olarak, üç morfolojinin tamamı, gerçek bir süper kapasitör cihazında elektrot malzemesi olarak test edilmiştir ve cihazın performansı, özellikle spesifik kapasitans ve depolama mekanizması, nokta kusurları tarafından aracılık edilmiştir. Morfolojiye bağlı kusurlu ZnO elektrodu, EDLC'den psödosüperkapasitörlere kadar süperkapasitör cihazının çalışma prensibinin izlenmesini sağlar.

## **Acknowledgement**

It has been an absolute privilege for me to embark on this journey. I am thankful to Almighty God for this opportunity.

It has opened me up to a whole new world beyond my imagination. More so to raise my values and work ethic, in addition to opening doors for future pursuits and pathways.

I am deeply grateful to my supervisor, Assoc. Prof. Dr. Emre Erdem for being a guide and giving me the freedom to learn and grow at my own pace and leading me all through out when I needed direction.

Also, I am indebted to our collaborators who have generously contributed towards my journey in the past two years from SUNUM, TOBB Ankara, and in Università di Catania, Italy.

Finally, I am thankful to my family and friends without whom none of this would have been possible.

## Table of Contents

LIST OF FIGURES	vii
LIST OF TABLES	viii
LIST OF ABBREVIATION	ix
1. INTRODUCTION	1
2. CLASSIFICATION OF SUPERCAPACITORS	4
2.1 Electrochemical Double Layer Capacitors (EDLC)	4
2.1.1 Carbon Aerogels, Carbon Foams and Carbid-derived Carbon (CDC)	6
2.1.2 Graphene and Carbon Nanotubes (CNT)	6
2.1.3 Activated Carbon (AC)	8
2.2 Pseudocapacitors	8
2.2.1 Conducting Polymer Pseudocapacitors	9
2.2.2 Metal Oxide Pseudocapacitors	9
2.3 Hybrid Supercapacitors	10
2.3.1 Asymmetric Hybrid Supercapacitors	11
2.3.2 Composite Hybrid Supercapacitor (CHS)	11
2.3.3 Rechargeable Battery-type Hybrid Supercapacitors	12
3. SUPERCAPACITOR DEVICE DESIGN	14
3.1 Sample Synthesis	17
ZnO Crystal and Sample Nanostructures	17
Nanoparticles (NP) and Nanourchins (NU)	19
Nanoflowers (NF)	20
3.2 Methods	22
4. RESULTS AND DISCUSSION	25
4.1 X-ray Diffraction Analysis (XRD)	25
4.2 SEM	27
4.3 Raman Spectroscopy	28
4.4 Photoluminescence Spectroscopy	32
4.5 UV-Vis Spectroscopy	34
4.6 EPR Spectroscopy	35
5. SUPERCAPACITOR DEVICE TEST	39
5.1 Electrical Impedance Spectroscopy	39

5.2 Cyclic Voltammetry	40
6. CONCLUSIONS	43
7. FUTURE WORKS	45
8. REFERENCES	46

## LIST OF FIGURES

<b>Figure 1.</b> The flow of energy and the placement of supercapacitors in it.....	2
<b>Figure 2.</b> Overview of the types and classification of supercapacitors.....	4
<b>Figure 3.</b> Classification of electrochemical double layer capacitors (EDLC) <sup>1</sup> .....	5
<b>Figure 4.</b> Classification of pseudocapacitors. <sup>1</sup> .....	9
<b>Figure 5.</b> Classification of hybrid supercapacitor into three types according to their design or working mechanism. <sup>1</sup> .....	11
<b>Figure 6.</b> The <i>top</i> part of the figure shows the schematic for the asymmetric supercapacitor design. The photograph at the <i>bottom</i> displays the actual setup built during the experiment. ....	14
<b>Figure 7.</b> An overview of the focus and loci of the active material in our device. The schematic circuit diagrams represent of a rough estimation of two capacitors in series and the sudden jump in their capacitances at the surface level of the active electrode. ....	15
<b>Figure 8.</b> The hexagonal wurtzite ZnO crystal structure. <sup>52</sup> .....	18
<b>Figure 9.</b> The preparation method for nanoparticles.....	19
<b>Figure 10.</b> The steps and procedures taken to produce nanourchins.....	20
<b>Figure 11.</b> The step taken during preparation of nanoflowers. ....	22
<b>Figure 12.</b> Powder X-ray diffraction patterns of ZnO nanostructures. All the indexed peaks in the obtained spectra are matched with the planes of the ZnO hexagonal wurtzite structure (01-079-0207) .....	26
<b>Figure 13.</b> Structural and morphological investigation of different ZnO nanostructures. a) EDS spectra of three different nanostructures. The analyses were conducted at 18keV accelerating voltage. b) Secondary-electron SEM micrograph of ZnO nanoflowers, c) Secondary-electron SEM micrograph of ZnO nanourchins, and d) Secondary-electron SEM micrograph of ZnO nanoparticles. All images were recorded through an in-lens detector with an accelerating voltage of 5 keV. In the inset, higher magnification of each image is given.....	28
<b>Figure 14.</b> First order and second order Raman spectra of three different ZnO nanostructures ( $\lambda=532\text{nm}$ ). ....	29
<b>Figure 15.</b> The PL intensity versus energy graphs (a-c) for the different ZnO nanostructures. ....	33
<b>Figure 16.</b> Tauc-plots (d-f) obtained from UV-Vis reflectance spectra for the different ZnO nanostructures. ....	34
<b>Figure 17.</b> (a) Intensity measured at room temperature X band (9.47Hz) EPR and (b) plot of EPR peak to peak intensity with respect to $P^{1/2}$ for the hydrothermal processed three different nanostructures of ZnO.....	36
<b>Figure 18.</b> The electrochemical behavior of three produced supercapacitors investigated by EIS in Nyquist plot of the supercapacitors.....	39
<b>Figure 19.</b> Investigation by behavior of charge-discharge (intercalation-deintercalation) via the cyclic voltammetry (CV) for observing the electrochemical behavior of three produced supercapacitors.....	40

## LIST OF TABLES

<b>Table Number</b>	<b>Caption</b>	<b>Page No.</b>
Table 1	Table 1 Summarized traits of the various ZnO nano-scale architectures used as electrodes for supercapacitors1.	16
Table 2	All the possible crystal structures of ZnO. The first row is the ZnO wurtzite crystal structure which our samples contain. 51	18
Table 3	Table 3. Room temperature frequencies and symmetries of the first-order and second-order Raman spectra observed in different ZnO nanostructures. Parentheses indicate symmetries that although being present in the spectra display a much lower intensity than the dominant one.	31
Table 4	Provides a summary of the result obtained from the PL graphs.	33
Table 5	Different recorded parameters for core and shell of the various ZnO nanostructures.	37

## LIST OF ABBREVIATION

NU	Nanourchins
NF	Nanoflowers
NW	Nanowires
XRD	X-Ray Diffraction
SEM	Scanning Electron Microscopy
UV-Vis	Ultraviolet Visible Spectroscopy
PL	Photoluminescence Spectroscopy
EPR	Electron Paramagnetic Spectroscopy
EIS	Electron Impedance Spectroscopy
CNT	Carbon Nano Tube
CHS	Composite Hybrid Supercapacitor
CV	Cyclovoltammetry
SWNT	Single Walled Nano Tube
MWNT	Multi Walled Nano Tubes

## 1. INTRODUCTION

Batteries and capacitors are known as energy storage systems. Batteries are preferred for applications with high energy density but with limited power output requiring long-term use of energy while capacitors are preferred in applications where energy is required to be delivered with high power densities. Both batteries and capacitors are insufficient for applications requiring high energy and power density. This leads to an intensive investigation of the new type of energy storage systems known as electrochemical capacitor, supercapacitor or ultracapacitor. Supercapacitors are produced to contribute towards finding solutions for storing energy that in rise for the energy demand present today. The fundamental reason behind such device-development-oriented research is for the transition from fossil fuels to renewable energy resources. On the other hand, as important as energy production is, the question of how the energy will be stored, its efficiency and minimizing the environmental impact are also some of the critical challenges in this research. Accordingly, supercapacitors have plenty of applications in industrial fields mostly for device memory in electronics and automotive industry which for rapid acceleration, with a long product lifetime; it benefits from high specific capacitance values, fast charge-discharge peculiarities and promising storage capabilities. There is an ongoing development in supercapacitor technology and research, due to their improved energy density values, and a promising hope that supercapacitors could turn out to be further closer to an alternative than conventional batteries are <sup>1-3</sup>. The goal is where the energy harvesting system can supply and store both high energy and provide high output power just by combining the multi-functional advanced materials as electrodes with smarter designs. As mentioned above, today the energy density of supercapacitors is much lesser than the chemical power sources, but the power density is much higher of that. The performance of low-cost and eco-friendly energy conversion and storage components which are mostly requirements of the electrical energy storage systems, such as batteries and electrochemical capacitors depends on the physical and chemical properties of electrode materials. The creation of the next generation energy storage and conversion devices will depend on engineering them to reach that goal. The pronounced impact of supercapacitors is entirely based on the double layers, where the capacitance originates from the pure electrostatic charge accumulated at the electrode/electrolyte interface, thus the capacitance value strongly depends on the surface area of the electrode

materials that is reachable to the electrolyte ions. The capacitance of supercapacitors is defined by electrostatic double layer capacitance or electrochemical pseudocapacitance resulting from reversible reduction and oxidation (redox) reactions or intercalation. A supercapacitor which uses both mechanisms simultaneously is called hybrid supercapacitor. Additionally, the cycle life of such supercapacitors is extraordinarily long, they are nearly free of maintenance, have a higher power density, can be charged at high rates, and are much safer than the batteries.

The progress of supercapacitor technologies continues mostly on the development of nanostructured electrode materials. From the morphology point of view, to develop high-performance electrode materials, scientists have designed and integrated one-dimensional (1D) (nanotubes, nanowires), two-dimensional (2D) (nanosheets, nanodiscs), and three-dimensional (3D) nanoarchitectures into electrode materials for the production of supercapacitors and batteries as well. As it is seen, both materials synthesis and the design of the storage and harvesting systems are playing a vital role to obtain high-performance from the device.

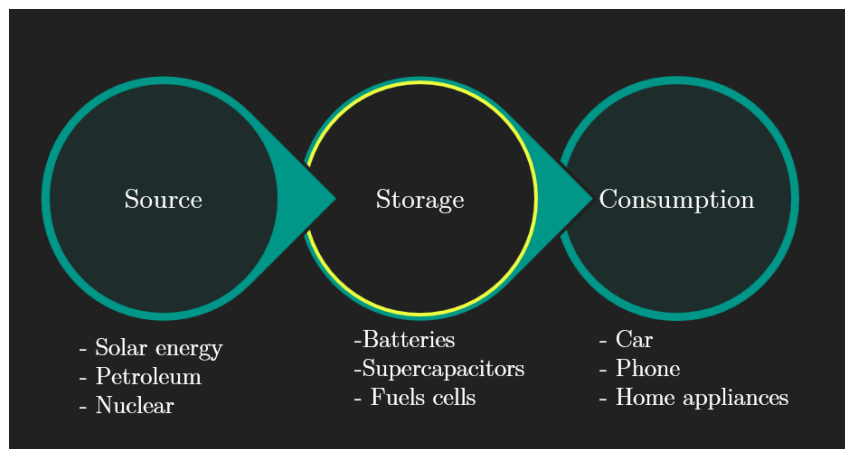


**Figure 1:** The flow of energy and the placement of supercapacitors in it.

In this thesis, we will have two aspects of supercapacitor research. Firstly, we will visit the Classifications of Supercapacitors. This is where we explore on the three main types of Supercapacitors namely EDLC, Pseudo Supercapacitors and Hybrid Supercapacitors. After which, we shall also take a look at sub categories with examples and detailed advantages and

limitations of each type. Secondly, from Chapter 3 we will take a look at ZnO as an electrode material and then delve into the designing aspect of morphologically varied ZnO electrodes to build asymmetric hybrid supercapacitors. In Chapter 4, we will present the results that have been obtained from the Materials Characterization of the samples that have been produced. Here we will study how morphology causes a difference in each of the characterizations result. In Chapter 5, we will create an asymmetric hybrid supercapacitor and test its performance via Electrical Impedance Spectroscopy and Cyclic Voltammetry.

## 2. CLASSIFICATION OF SUPERCAPACITORS

Supercapacitors can be classified into three categories based on the mechanism for storage and their working principles.

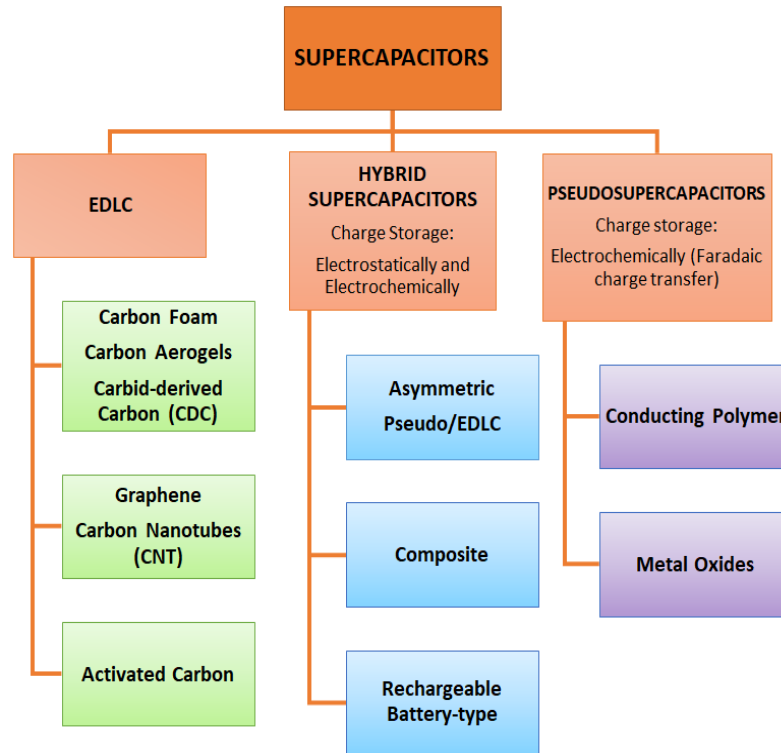


**Figure 2.** Overview of the types and classification of supercapacitors.

### 2.1 Electrochemical Double Layer Capacitors (EDLC)

The working principle of EDLC is based on electrostatically stored charges. The fundamental equation for all capacitors is given by:

$$C = \frac{\epsilon_0 \epsilon_r A}{d} \quad 1$$

where,  $A$  is the surface area of the electrode;  $\epsilon_0$  is the permittivity of free space;  $\epsilon_r$  is the relative permittivity of the dielectric material, and  $d$  is the distance between two oppositely biased electrodes.

According to the fundamental relation given in equation 1, the capacitance of a standard capacitor can be raised by the increase in the dielectric constant of the material, surface area and the decrease of interplanar thickness. However, such an increase can be made further by modifying the materials system and capacitor design. For instance, one may change the

particle size to the sub-nanometer scale where the quantum confinement limits are almost reached. This leads to the material having extraordinary electrochemical performance. Alternatively, metal ion doping i.e., Fe, Mn, Cr, Co may increase the electrical conductivity of the electrode material which consequently increases the capacitance as well which applies to the design of the capacitors. For instance, if a capacitor has symmetric electrodes or its working principle is based on faradaic reactions this supercapacitor can eventually have enhanced electrochemical performance. In short, the faradaic process occurs when Faraday's Law is observed, meaning during this process charge transfer occurs across the electrode-electrolyte interface. Whereas in the non-faradaic process, which is addressed after this, is where Faraday's law is not obeyed i.e. charge transfer does not occur, e.g. adsorption-desorption at the electrolyte-electrode interface, solvent dipole reorientation Figure 3 the main classification of EDLC is given that is partly based on Figure 2.

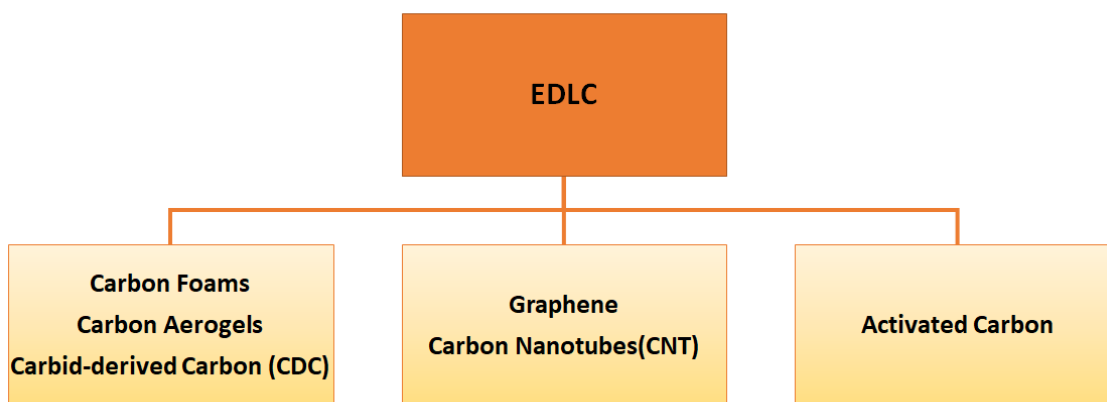


**Figure 3.** Classification of electrochemical double layer capacitors (EDLC)<sup>1</sup>.

There are plenty of pros and cons while speaking of EDLC devices but we focus on the fundamental features. For instance, charging and discharging cycles are highly reversible due to its non-faradaic electrical mechanism. This also gives an extremely stable cyclic ability up to  $10^6$  cycles or more, high rate of charging and discharging, and finally little degradation. The main drawback of EDLC is the limitation in the selection of the electrode materials. While in EDLC devices it is necessary to use highly conductive electrodes. Such shortcoming can be solved by the recent development of ionic conductive electrolytes. That is why the

investigation of ionic electrolytes, in particular solid ones, are a trending hot topic nowadays<sup>2-4</sup>. There are three main types of EDLC in terms of the carbon content which leads to different function or role in the device. One may distinguish such useful functions by the properties of carbonaceous materials i.e. morphology, hybridization and structural defects:

1. Carbon Aerogels (nanopores), Carbon foams (micropores) and Carbid-derived carbon (CDC) (controllable pore size)
2. Carbon nanotube (CNT), graphene
3. Activated Carbon

### **2.1.1 Carbon Aerogels, Carbon Foams and Carbid-derived Carbon (CDC)**

Carbon Aerogels are known to be one of the world's lightest material, with a high surface area and a density of  $200 \mu\text{g}/\text{cm}^3$ <sup>5</sup>. It displays great thermal, electrical and mechanical properties with a high focus on high compressibility and adsorption level. This has made it a potential successor in the cleaning of any major toxic solution and oil spillage, as it can adsorb liquid oil 900 times its mass<sup>5</sup>. Although its light-weight structure could be strengthened by a polymer binder, it instead turns into a poor conducting structure. The traditional methods to create amorphous carbon aerogels include sol-gel processes, freeze drying of carbon suspensions. But today, the typical carbon aerogel consists of a fine 3D network of CNT with an increased Young's modulus i.e. super compression and elasticity in addition to its existing mechanical properties<sup>6</sup>. It has enhanced its mechanical and transport properties, despite its delicate appearance, supported entirely by Van der Waals forces between adjacent CNT. This serves as a prospective lightweight energy storage device, also, as a potential fine detector of deformation in any slight changes in pressure<sup>7</sup>. A fall in its flexibility can result in a carbon aerogel as cracks may emerge during continuous cyclic compression. Different preparation methods allow control of the concentration of the pores independently, making carbon aerogel a suitable electrode material. However, if the metal precursor is included it results in a change in pH, pyrolysis, activation etc., making it difficult to manipulate pore consistency<sup>8</sup>.

### **2.1.2 Graphene and Carbon Nanotubes (CNT)**

Graphene is a special kind of graphite consisting of a monolayer of carbon atoms of atomic thickness. As it displays outstanding electrical and mechanical properties, it is prevalent and

popular through preparations using a variety of techniques. Another reason for its regard is its ability to recombine with different functional groups into its structure to display a wide array of electrical and mechanical properties. Graphene allows in creating flexible structural dimensions whether in 0D, 1D, 2D, 3D thus providing a desired finely tuned surface area, enhancing the desired structure. Some different examples include graphene quantum dots, fibre, yarn-like graphene, graphene film, graphene foam and carbon aerogels. As graphene itself is a leading material having high electrical and thermal conductivity, strong mechanical strength and chemical stability. These properties would like to be embedded in the constructed supercapacitor along with high power density, charge/discharge rate and long-life cycle performance.

Graphene also can form numerous nanocomposites with other elements or functional groups to form graphene conductive polymer, graphene with metal oxide, graphene hydroxide. These nanocomposites allow multiple characteristics to be constructed including higher specific surface area, higher power density, tractable pore size, electrical conductivity etc. Although, challenges lie with these composites having their own distinct characteristics, some of which may not contribute to the capacitance or may cause a decrease in overall effective diffusion of ions. Even compromising properties emerge, for instance, a graphene nanocomposite of higher conductivity at the cost of its mechanical strength<sup>9</sup>. In simple words, a graphene sheet practically rolled up would form a CNT. They are known to be highly conductive. This conduction in CNT occurs via ballistic transport, this means the charge carriers have a very high mean free path, and faces no scattering therefore, no joule heating takes place. Joule heating, or the heating up of conductors while conducting electricity is a major problem in other conductors. But CNT has a huge advantage in this aspect. CNT are mainly of two types, Single Walled Nano Tube (SWNT) and Multi Walled Nano Tubes (MWNT). SWNT have high flexibility and surface area with sizes of around 5nm. Despite it having these highly sought-after properties, are difficult to handle. This is due to its tendency to get entangled to form bundles. They are cumbersome to isolate and do not share the same properties to that of an immaculate SWNT. MWNT on the other hand, contains large number of defects in their structure compared to that of SWNT. This would result in a change in their structure and ultimately deviating from its intrinsic properties, resulting in higher resistance. But they are longer in size compared to SWNT, with an average length of

20 nm and have a greater volume than SWNT and therefore act as an ideal filler material. Although CNT is claimed to have properties highly sought after, it is their composite forms that are chemically modified and reinforced CNT versions which are of finest grade with heightened strengths. Processes utilized in preparing such varied versions of CNT include solution processing, melt processing, compression moulding, chemical vapour deposition methods to build modified samples like that of melt processed fibres, CNT composites, CNT composite fibres etc <sup>10</sup>.

### **2.1.3 Activated Carbon (AC)**

EDLC devices based on activated carbon electrodes can show superior electrochemical performance not only due to their high surface area but also because of their oxidizing behaviour. Oxidizing of carbon materials in general results in the merging or strongly overlapping of D and G band of Raman bands which affects the phonon density of states. This also causes an obvious red shift in Raman lines. Such behaviour can be described by the extensive controlling of pore size, thus the defect structures such as carbon dangling bonds and C-C bonds. In activated carbon the bonus part is the low cost compared to graphene. Also, activated carbons enable extensive control of pore sizes ranging from below 5 nm to greater than 50 nm. Probably the main drawback of activated carbon electrodes is that the different porous structure does not always contribute towards a high capacitance, due to mismatch of electrolyte ion sizes. As a matter of fact, pore size and ion size of an electrolyte are directly correlated with each other and synergy between these two parameters gives the optimum electrochemical performance in a capacitor. Of course, at this point defect structures of the electrodes play additional crucial roles in the determination of the whole device performance <sup>11-13</sup>. Thus, to avoid low storage of charge capacity one has to find the best matching of electrolyte ion size and pore size <sup>14, 15</sup>. Recent supercapacitor studies of activated carbon electrode can be found in elsewhere <sup>13, 16-18</sup>.

## **2.2 Pseudocapacitors**

These capacitors are faradaic, undergoing redox reactions i.e. charge transfer occurs between electrolyte and electrode. They are prepared using different methods including electrospin,

redox, intercalation processes. This faradaic process leads to pseudo-capacitors having higher energy densities than EDLCs. Most electrode materials of this type of capacitor include metal oxides, metal-doped carbon and conductive polymers<sup>19</sup>. However, pseudocapacitors also have a shorter life cycle and power density. These results occur due to the redox reactions in the capacitors<sup>20</sup>.

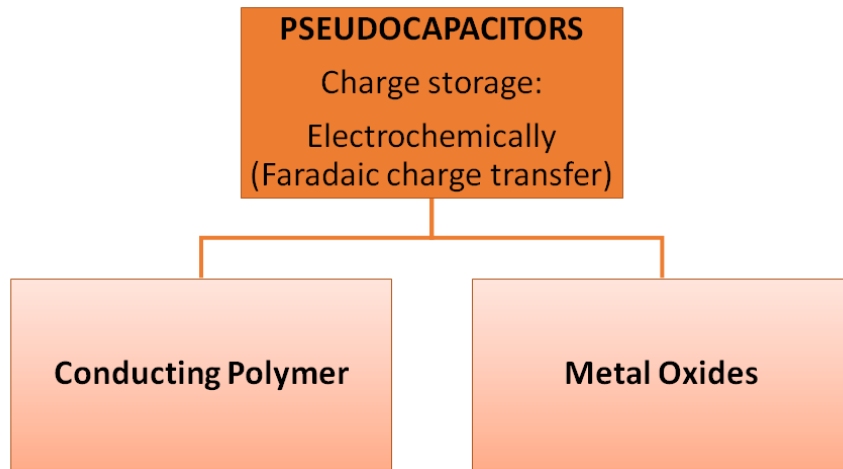


**Figure 4.** Classification of pseudocapacitors.<sup>1</sup>

### **2.2.1 Conducting Polymer Pseudocapacitors**

These types of supercapacitors display high capacitance, high conductivity i.e. low ESR and cost compared to carbon based EDLCs. They are said to have great potential densities and some example materials include polypyrrole, polyaniline, polythiophene<sup>14</sup>. Attributable to its flexibility and conductivity it is commonly used to improve capacitance as a nanofiller with reportedly higher areal capacitance than EDLC<sup>21</sup>. Polymer based electrodes normally have lower cycle stability than carbon based electrode. When doped, polymers can boost conductivity on one hand though they also display a change of volume, causing swelling and rise in the thickness of the electrode, a hazard for any device<sup>21</sup>.

### **2.2.2 Metal Oxide Pseudocapacitors**

These materials provide very high conductivity. One of the most researched metal oxide is RuO<sub>2</sub>. It also has low Equivalent Series Resistance (ESR) and very high specific capacitance. But its high cost compared to other transition metal oxides has caused researches to diverse

into alternate possibilities. However, metal oxides are said to yet achieve their potential capacitance values. Some of the processes included in their fabrication process include insertion, intercalation, sol-gel, anodic deposition, spray deposition, hydrothermal synthesis, oxidative synthesis etc.<sup>22</sup>. Metal oxides itself are claimed to provide high capacitance with high energy at a low current density. Though, metal oxides are said to cause cracking of electrodes leading to short term stability. As their pores cannot be designed or altered in any form<sup>23</sup>. In general, they are combined with carbon to form composites to counterbalance these traits. In addition, carbon-based materials are devoted as the electrode materials for designing pseudocapacitor electrodes and the combination of them with nanosized transition metal oxide materials, were shown to have potential to achieve ultrahigh values of specific capacitance such as  $\text{Co}_3\text{O}_4$ ,  $\text{MnO}_2$ ,  $\text{Fe}_3\text{O}_4$  and  $\text{ZnO}$ . In this thesis, the synergetic effects of  $\text{ZnO}$  nanoarchitecture and the counter electrode will be inspected in detail.

### 2.3 Hybrid Supercapacitors

This type of supercapacitor consists of polarizable electrodes (carbon) and non-polarizable electrodes (metal or conducting polymer) to store charges. It uses both faradaic and non-faradaic processes<sup>14</sup>. i.e. making use of these properties to obtain high energy storage through both battery type and capacitor type electrode<sup>22</sup> resulting in better cycling stability and lower costs than EDLCs. It has three main categories: asymmetric, composite, battery-type as illustrated in Figure 5.

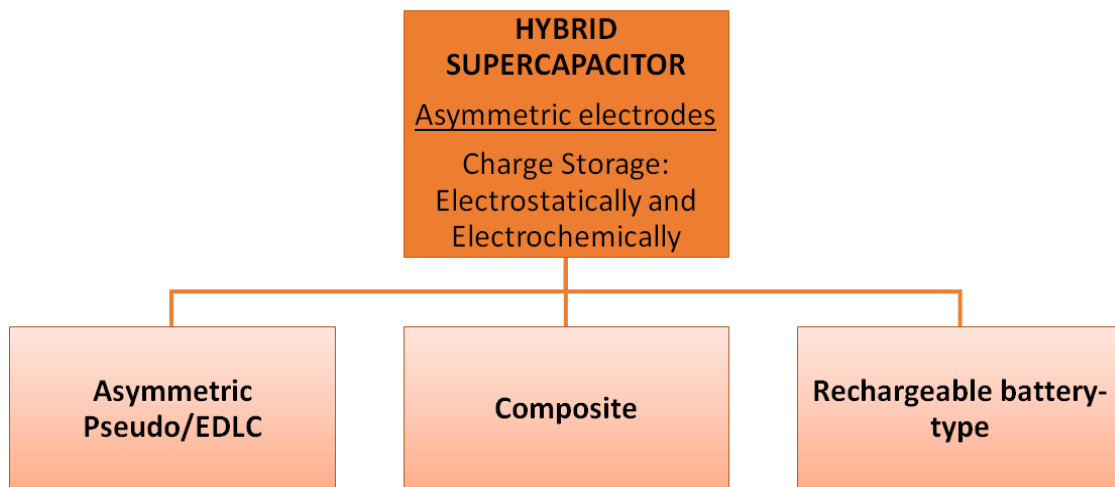


**Figure 5.** Classification of hybrid supercapacitor into three types according to their design or working mechanism.<sup>1</sup>

### **2.3.1 Asymmetric Hybrid Supercapacitors**

Amongst other supercapacitors, this type is distinctive for its two dissimilar electrodes. They are designed to work simultaneously to address the power and energy density requirement, as one works as a capacitive electrode and the other as a faradaic electrode. Mostly carbon derived materials serve as the negative electrode while a metal or metal oxide electrode for the anode. Metal electrodes are said to have high intrinsic volumetric capacity leading to a rise in the energy densities<sup>24</sup>. These types of capacitors have the potential to display higher energy density and cycling stability than that of symmetric supercapacitors. This is the case seen for carbon and MnO<sub>2</sub> on Nickel foam based electrode<sup>25</sup>. Self-discharge of a capacitor is a confronted question in all capacitors. One way to tackle it is to incorporate in the asymmetric capacitor, the simple rocking-chair mechanism. Here is where the maximum potential is ensured at zero current<sup>24</sup>. Almost all electrolyte overtime causes depletion of ions and electrodes which decreases the conductivity along with a rise in the internal resistance, the newly designed electrolytes could feasibly evade this pressing concern. Another challenge is to increase the working voltage of supercapacitors. If the negative electrode activated carbon or carbon derived sample effectively p-doped, it has the scope in improving voltage range along with the rocking-chair mechanism. The carbon microporous layout is also a critical feature to be perfected. Once amended it would allow convenient ion transport to raise the capacitance of the device<sup>24</sup>.

### **2.3.2 Composite Hybrid Supercapacitor (CHS)**

The purpose of composites hybrid supercapacitors is to have synergistic outcomes of specific capacitance, cyclic stability, high conductivity. As seen in EDLC above, carbon based supercapacitors have a great surface area, no joule heating, low resistance, great mechanical strength. However, carbon itself shows a poor energy density than the commercially used lead acid battery and lithium ion battery. Whereas, metal oxides, which are being investigated have poor conductivity, with the exception if RuO<sub>2</sub>, experience joule heating, with poor surface area, poor structural stability when undergone strain. But it is competent in storing charge, thus the energy. Composite Hybrid Supercapacitor intermingles the two, a composite

which will simultaneously merge to provide the synergistic characteristics of both carbon and metal oxide that are sought after. Which include that of specific capacitance, cyclic stability, high conductivity. Together carbon will provide a channel for charge transport and the metal oxide will store charge via redox reactions contributing to high specific capacitance and high energy density. While the conductivity of the composite is highly tunable, as it depends on the structure of the carbon whether microporous, or, mesoporous and or, macroporous <sup>26</sup>. Which means pore diameter is an essential factor to consider as it determines if the ions will or will not be adsorbed to the surface of the electrode, defining its EDLC characteristic for charging/discharging. If not, there will be low conductivity for it. There are limitations of the composites as well for example when vanadium oxide was layered on carbon nanofibers, the efficiency started to decrease when the layer became thicker (18 nm) <sup>27</sup>. This has arisen due to an imbalance between the redox site and conductivity of the composite itself. Also, another challenge arises when the successive ion diffusion declines, due to protruding nanowhiskers that grow on the carbon nanofibres, even though, the surface area of the metal oxide increases <sup>28</sup>. This indicates how the limitations and benefits of the composites are highly dependent on the constituents itself, their combinations and the electrolyte which is beyond the scope of this study.

### **2.3.3 Rechargeable Battery-type Hybrid Supercapacitors**

The prospects of this category of supercapacitors are in striving up through the midway diagonal of the Ragone plot which holds promising traits of higher specific capacitance, energy density and power density that still need to be excelled towards, than that of present supercapacitors. Some considered factors discussed here, include that of surface modification, synthesis of the perfect nanocomposite material and microstructure optimization. As the creation of electroactive nanoparticles leads to faster reactions the electrolyte, it should effectively lead to faster reactions, by undergoing redox with electroactive nanoparticles, as mentioned before in this study. However, a challenging matter rises because it is also possible it will face spurious reactions with the electrolyte as well. In building nanocomposite materials some metal oxides multiple challenges arise. One of them,  $\text{LiMnPO}_4$ , have a higher potential than its Fe counterpart, then again are difficult to coat with a carbon layer like  $\text{LiFePO}_4$ . But a remarkable strategic approach to overcome it was by,

creating a multi-layered structure of carbon layered over Fe over Mn, which did the trick. In fact, the study mentions it performed better than expected at higher rates and without any direct contact of the oxidizing Mn metal oxide to the electrolyte itself<sup>29</sup>. Electroactive species are prized for their privilege to give in faster electrode reactions. One enhancing technique lies in developing granules in disproportioned fractions on the electrode surface. And so 'fractal-granularity', at the electrolyte-electrode interface causes a higher surface area exposure leading to greater prospects for in rising of energy. Another major improvement lies in applying the double layer concept to this type of supercapacitor. It creates a Helmholtz double layer where the charge is stored at the interface between the carbon electrode and the electrolyte. It occurs due to like charges being repelled from, at the interface and attraction of counter-ions, causing a physical charge storage mechanism to occur simply from the upsurge of polar ions. This had an effect of changing the energy density in this study by several orders of magnitude.

In this thesis we have analyzed the classification of supercapacitors with regards to electrode, fabrication and design. As observed, there are multiple factors and parameters, each playing a role in the device built. Some of which include the energy density, power density, adsorption, compressability, internal resistance, defects in crystal structure. Our focus shifts to ZnO based asymmetric hybrid supercapacitors, as we believe it synergistic effect combines the wide band gap, defects structure present, electron mobility to provide a high capacitive property.

Nevertheless, despite the prospect of new tools and emerging software for computations it is safe to say, similar working principles also take place in devices of other types with different materials due to the same yet crucial electrochemistry and physics behind it.

### 3. SUPERCAPACITOR DEVICE DESIGN

The next generation innovation for supercapacitors lie in the design and material of the electroactive electrode at the nanoscale level, where actual mechanisms of electric storage take place. And manipulating the architecture to our needs could potentially raise the capacitance of the device by several orders of magnitudes (Figure 7). This makes it an important area for exploration and understanding behind the mechanisms that take place here.

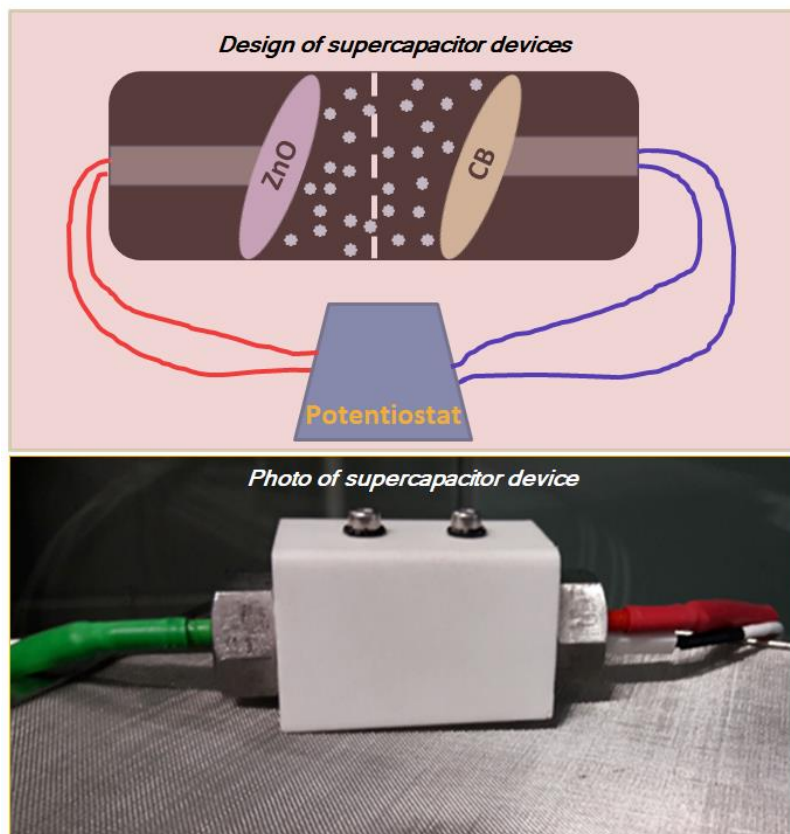


**Figure 6.** The *top* part of the figure shows the schematic for the asymmetric supercapacitor design. The photograph at the *bottom* displays the actual setup built during the experiment.

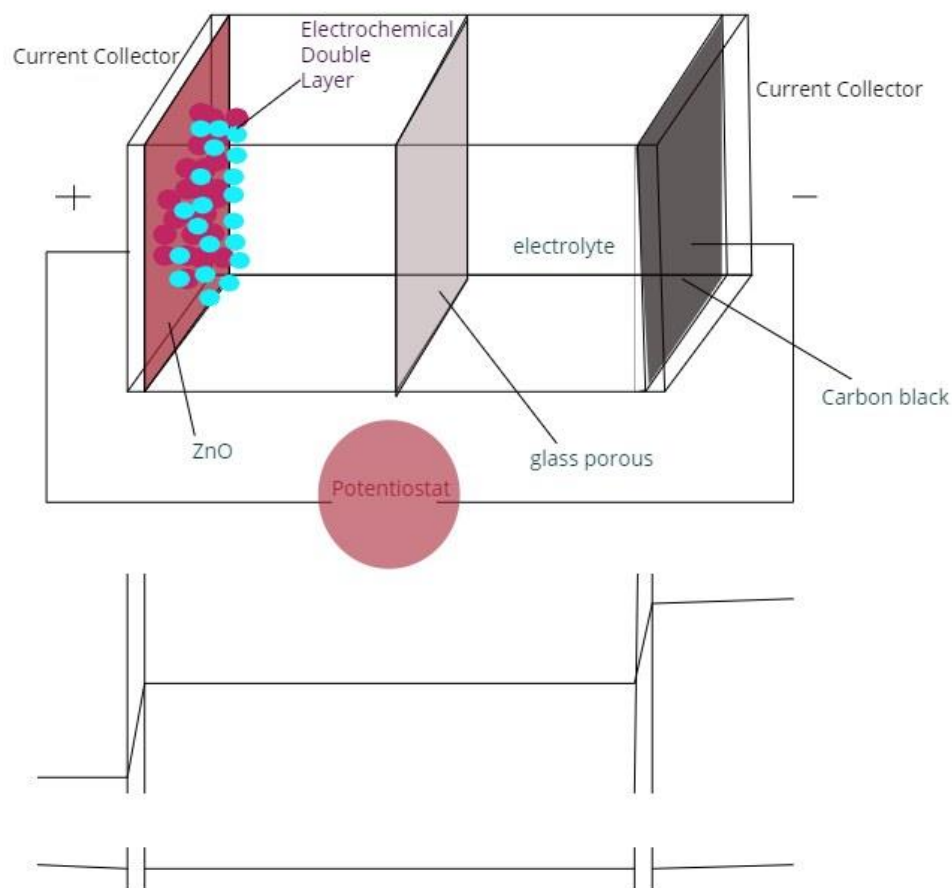


**Figure 7.** An overview of the focus and loci of the active material in our device. The schematic circuit diagrams represent of a rough estimation of two capacitors in series and the sudden jump in their capacitances at the surface level of the active electrode.

In our device (Figure 6), ZnO and carbon black materials were used as electrodes without any additives such as polymeric binders or carbon materials. This means there is no slurry phase in the present supercapacitor design. In order to test the performance of ZnO and dependency of morphology and defect centers only asymmetric supercapacitor was designed being one electrode ZnO and the other electrode is carbon black. WHA1825042-Whatman® glass microfiber filters, Grade GF/F, were used as the dielectric separator; these filters are highly porous and effective to separate the two electrodes. Finally, well-known 1 M LiPF<sub>6</sub> (lithium hexafluorophosphate) dissolved in 50/50 (v/v) mixture of ethylene carbonate and diethyl carbonate EC/DMC (Aldrich) electrolyte was used to get a wide range of voltage window.

The full cell supercapacitors with LiPF<sub>6</sub> as the electrolyte were assembled in a glove box filled with Ar ([O<sub>2</sub>] < 0.5 ppm). The full cell design is illustrated in Figure 6. These designs were successfully implemented in former studies based on superbat<sup>30</sup>, octacalcium phosphate<sup>31</sup>, carbon dots<sup>32, 33</sup>, and high energy ball milled ZnO/graphene foam<sup>34</sup> electrodes.

**Table 1** Summarized traits of the various ZnO nano-scale architectures used as electrodes for supercapacitors<sup>1</sup>.

Sample System	Specific Capacity	Size	Capacitor type
nanocluster	2176 F/g	20 nm	Hybrid Supercapacitor <sup>35</sup>
nanoflower	203 F/g	1-2 μm	EDLC and Pseudocapacitor <sup>36</sup>
fabric	40 F/g	-	Hybrid Supercapacitor <sup>37</sup>
nanowire	260 F/g	$d= 300$ $l= 100 \mu\text{m}$	Pseudocapacitor <sup>38</sup>
nanoparticle	341.6 F/g	32.30 nm	EDLC <sup>39</sup>
nanocomposite	123.8 F/g	-	EDLC <sup>37</sup>
nanocomposite	314 F/g	5-10 nm	Pseudocapacitor <sup>40</sup>
nanorod	51.6 F/g	$d= 50-100 \text{ nm}$ $l=1 \mu\text{m}$	EDLC and Pseudocapacitor <sup>41</sup>
nanosphere	630 F/g	106 nm	EDLC <sup>42</sup>
nanoparticle	160 F/g	10-30 nm	Pseudocapacitor <sup>43</sup>
nanocomposite	122.4 F/g	30-70 nm	Pseudocapacitor <sup>44</sup>
nanotube	347.3 F/g	$d= 40-60 \text{ nm}$ $l= 0.5-2 \mu\text{m}$	EDLC, Pseudocapacitor <sup>45</sup>
nanorod	-	$d= 200 \text{ nm}$	Pseudocapacitor <sup>46</sup>
nanocomposite	155 F/g	-	EDLC and Pseudocapacitor <sup>47</sup>

nanofiber	178.2 F/g	$d= 150$ nm	EDLC and Pseudocapacitor <sup>48</sup>
nanotube	306 F/g	$d= 19.3$ nm	EDLC and Pseudocapacitor <sup>49</sup>
nanoparticle	352.9 F/g	15 nm	Pseudocapacitor <sup>50</sup>

The outline of this thesis starts with a big picture of where Supercapacitors stand and their importance. In chapter 2, we discuss the classification of supercapacitors. Each branch is separately considered with their sub-branches studied briefly. In our review paper <sup>1</sup>, we study the specific capacitances with widely varied nanoarchitectures for ZnO, ranging from nanoclusters, nanorods, nanocomposites which also display a wide range of specific capacitances with different designs of supercapacitors, discussed in Chapter 3. The study conducted has furthered our interest to investigate the effect of morphology on the performance and capacitance in designing an asymmetric hybrid supercapacitor. Three different nanomorphologies are chosen, tested and analyzed by different characterization methods to understand and determine their optical, electronic and structural properties revealed in Chapter 4, Results and Discussion. Our designed Asymmetric Hybrid Supercapacitor is then put to test in Chapter 5, via Cyclovoltammetry and Electrical Impedance Spectroscopy. It can be seen the evolution of supercapacitors continue with many factors in play, with combining the traits of batteries and capacitors remaining at heart, maximizing both its capacitance and electrochemical electrode performance through both EDLC and pseudocapacitance.

### 3.1 Sample Synthesis

#### ZnO Crystal and Sample Nanostructures

Experimentally there are three different available crystal structures that have been detected of ZnO: two cubic structures and one hexagonal wurtzite structure. The ZnO nanostructures for our samples is that of a hexagonal wurtzite crystal. Table 2 shows that computationally 13 possible crystal structures that could be present altogether. This was derived from ‘The Materials Project’, an innovative tool in the area for computational materials science. Our

samples are that of the hexagonal wurtzite crystal structure, as shown in Figure, in the first row.

**Table 2.** All the possible crystal structures of ZnO. The first row is the ZnO wurtzite crystal structure which our samples contain.<sup>51</sup>

Materials Id	Formula	Spacegroup	Formation Energy (eV)	E Above Hull (eV)	Band Gap (eV)	Volume	Nsites	Density (gm/cc)	
mp-2133	ZnO	P6 <sub>3</sub> mc	-1.799	0	0.732	49.719	4	5.438	<input checked="" type="checkbox"/>
mp-1986	ZnO	F $\bar{4}$ 3m	-1.791	0.007	0.631	24.82	2	5.446	<input checked="" type="checkbox"/>
mp-1093993	ZnO	P4 <sub>2</sub> /mnm	-1.776	0.023	0.741	104.228	8	5.188	<input checked="" type="checkbox"/>
mp-2229	ZnO	Fm $\bar{3}$ m	-1.651	0.148	0.724	20.421	2	6.62	<input checked="" type="checkbox"/>
mp-997630	ZnO	P6 <sub>3</sub> /mmc	-1.625	0.174	0.530	245.869	24	6.598	<input checked="" type="checkbox"/>
mp-1245209	ZnO	P1	-1.551	0.247	0.447	1085.013	80	4.984	<input checked="" type="checkbox"/>
mp-1245109	ZnO	P1	-1.549	0.25	0.403	1058.157	80	5.11	<input checked="" type="checkbox"/>
mp-1245015	ZnO	P1	-1.547	0.251	0.492	1118.338	80	4.835	<input checked="" type="checkbox"/>
mp-1017539	ZnO	P6 <sub>3</sub> mc	-1.498	0.3	0.448	49.084	4	5.508	<input checked="" type="checkbox"/>
mp-1245255	ZnO	P1	-1.401	0.398	0.921	1085.362	80	4.982	<input checked="" type="checkbox"/>
mp-13161	ZnO	Pm $\bar{3}$ m	-1.081	0.718	0.000	19.505	2	6.93	<input checked="" type="checkbox"/>

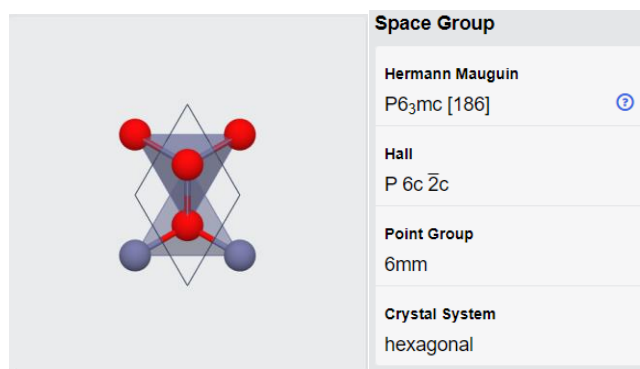


**Figure 8.** The hexagonal wurtzite ZnO crystal structure.<sup>52</sup>

## Nanoparticles (NP) and Nanourchins (NU)

Fabrication of ZnO NPs have been performed via a hydrothermal process in a solution containing 0.05 M zinc acetate dihydrate ( $\text{Zn}(\text{C}_4\text{H}_6\text{O}_4 \cdot 2\text{H}_2\text{O})$ ) as the zinc source and 1.0 M urea as the precursor. The pH value of the solution has been adjusted to precisely 4.8 with the acetic acid ( $\text{CH}_3\text{COOH}$ ). For the ZnO NU synthesis, the hydrothermal step has been carried out by using zinc nitrate hexahydrate ( $\text{Zn}(\text{NO}_3)_2 \cdot 6\text{H}_2\text{O}$ ) and urea of the same molarities. At this step, the pH adjustment has been conducted via dilute nitric acid and the pH value has been set to 4.5 strictly. Both of the prepared solutions have been kept in the oven at 80 °C for 3 h. The composed ZnO powders have been further filtered and washed several times to discard contaminations and dried in calcination oven at 300 °C for 30 min. at ambient air. All chemicals have been purchased from Sigma-Aldrich and have been used without further purification.

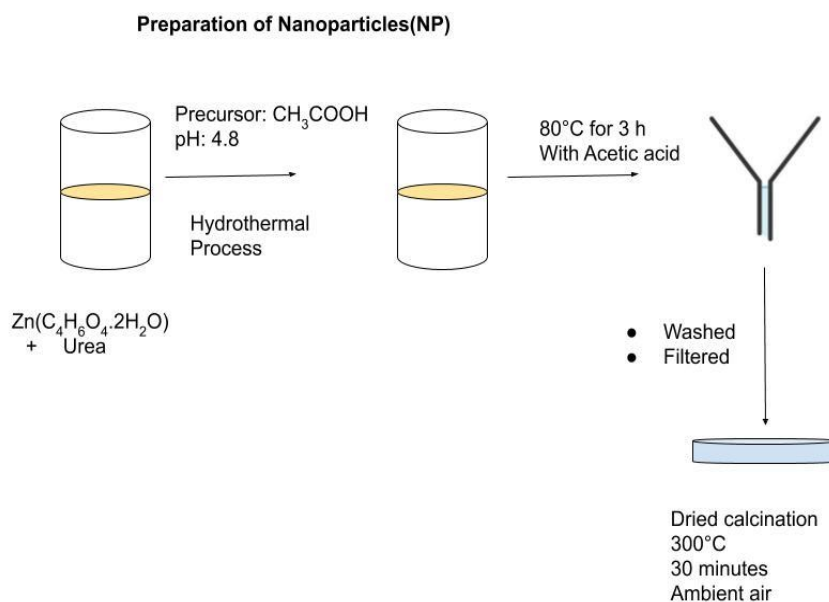


**Figure 9.** The preparation method for nanoparticles.

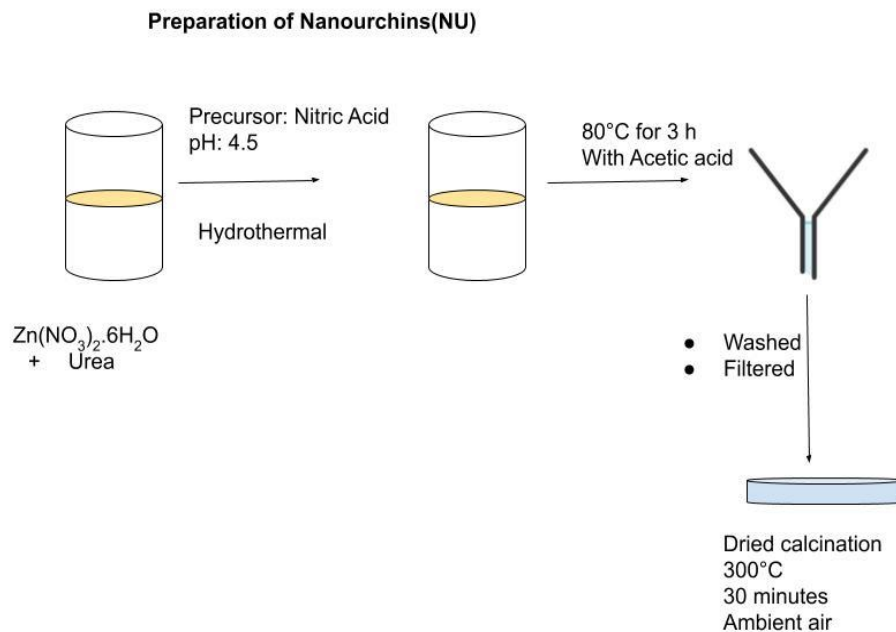


**Figure 10.** The steps and procedures taken to produce nanourchins.

### Nanoflowers (NF)

The synthesis process for one-dimensional ZnO NFs have also been conducted via the hydrothermal method in an aqueous solution containing 0.1 M zinc nitrate hexahydrate ( $\text{Zn}(\text{NO}_3)_2 \cdot 6\text{H}_2\text{O}$ ) and aqueous ammonium hydroxide solution (2% v/v). The reaction process has been kept for 1 h at 80 °C, and the formed powders have been washed and filtered for the proceeding annealing step conducted at 300 °C for 30 min. at ambient air. Here also, the chemicals have been purchased from Sigma-Aldrich and have been used without further purification.

ZnO nanostructure formation process can be divided into two main reaction steps which are

(I) nucleation

(II) growth<sup>53</sup>.

For the initiation of the primary nucleation step the supersaturation of the prepared ZnO solution should take place. This step is highly dependent on the solubility of the precursor material, which in the case of NP and NU is urea that has slow and gradual hydrolysis

kinetics in water<sup>54</sup>. This results in the realization of the following reaction steps that eventuate with the release of carbon dioxide and hydroxide ions into the reaction media:



It is highly essential to point out that the slow dissociation of urea causes a constant increase in the pH value of the solution during the 3 h reaction period. During this period, the reaction should not exceed the pH value of 9.0 for the successful precipitation to occur. Therefore, the arrangement of pH value prior to the reaction initiation is a crucial step for ZnO nanopowder synthesis. Moreover, the acidic pH adjustment of both NP and NU solutions results in the preferential transformation of carbonate ions into zinc carbonate hydroxide hydrate ( $\text{Zn}_4\text{CO}_3(\text{OH})_6 \cdot \text{H}_2\text{O}$ ) with heterogeneous nucleation sites providing various 3D nanostructure growth. Hereupon, the resulting nanostructure starts to depend only on the anionic source.  $\text{Zn}(\text{C}_4\text{H}_6\text{O}_4 \cdot 2\text{H}_2\text{O})$  standing for the anion source of NP structures has a tendency to be incorporated into the growing crystal during the reaction, while  $\text{Zn}(\text{NO}_3)_2 \cdot 6\text{H}_2\text{O}$  initiating the NU growth is featured as a non-complexing weak base. This type of anion is mostly adsorbed on the foretime grown crystal structure<sup>54</sup>. On the other hand, NF growth mechanism, due to its 1D orientation, varies from those of NU and NP. Ammonium hydroxide is selected as the precursor material providing both the  $\text{OH}^-$  and  $\text{NH}_4^+$  ions which serve as the oxygen source in ZnO and provide a buffering mechanism to form complexes with Zn ions<sup>55</sup>. The formation of complex hydroxyl species as a result of  $\text{OH}^-$  and  $\text{Zn}^{2+}$  initiates the nucleation step. Further control over the growth kinetics and mechanism is provided through ammonia ions, facilitating specific coordination which varies with the reaction parameters such as reaction temperature, solution concentration, and growth period<sup>56</sup>.

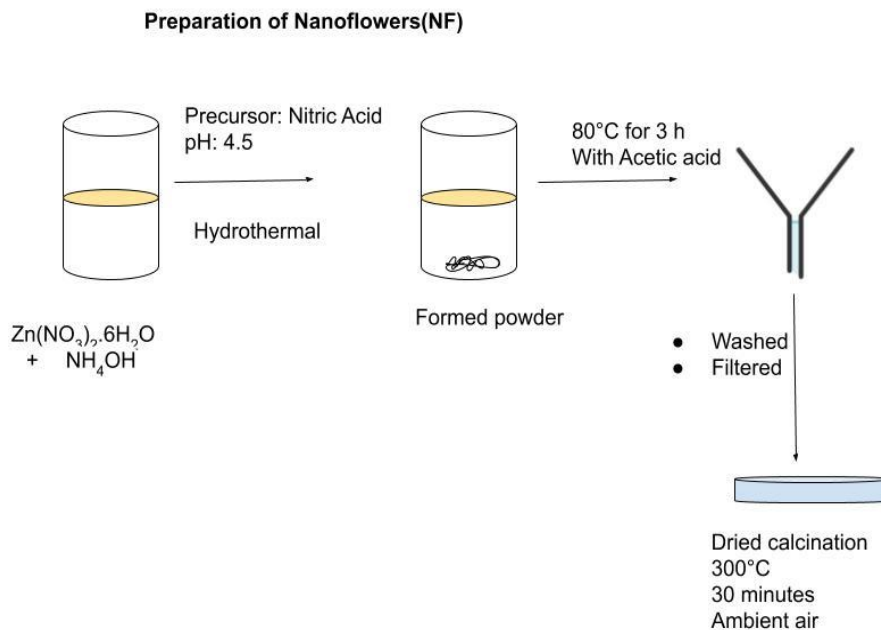


**Figure 11.** The step taken during preparation of nanoflowers.

### 3.2 Methods

#### XRD

XRD analyses were done using Bruker D2 Advance diffractometer utilizing Cu-K $\alpha$  ( $\lambda=1.54 \text{ \AA}$ ) radiation. The divergence slit size was fixed at  $0.5^\circ$ . Samples were scanned on the rotating stage between  $5^\circ$  to  $90^\circ$  using step size of  $0.02^\circ$  and time per step of 1 s. The X-ray diffraction (XRD) spectra were done using Bruker D2 advance diffractometer utilizing Cu-K $\alpha$  ( $\lambda=1.54 \text{ \AA}$ ) radiation. The divergence slit size was  $0.5^\circ$  and fixed.

#### SEM

Scanning Electron microscopy (SEM) creates intricate and detailed images of a sample by scanning a sample with a focused beam of electrons. The interaction of electrons with the surface by secondary electrons emitted by ZnO interacts with these electrons revealing information about the surface topography, composition. As secondary electrons have low energies they escape from the top few nanometers of the surface of the sample, making it a highly localized, making the surface image of the sample to have a very high resolution.

## **Raman Spectroscopy**

It is based on the Raman effect is an inelastic scattering process. When a change in polarizability occurs in a molecule, it detects vibrations providing information on its chemical nature, crystallinity, intrinsic stress and strain, structural fingerprint is used for its identifications. Raman was carried out using Renishaw InVia System coupled with a 532 nm green laser having random photon polarization. The as-synthesized materials were characterized by Raman Renishaw inVia Reflex. Raman data were collected using a 532 nm laser source with 2  $\mu\text{m}$  spot size within the range of 100-3000  $\text{cm}^{-1}$  in order to identify the nanoparticles. The UV transition and visible emission.

## **UV-Vis Spectroscopy**

Tauc's method is used to measure the bandgap of each of the nanostructures. Plotting software Origin was used to measure Tauc's plot. The bandgap measured is an approximate value determined by extrapolating a straight line when  $\alpha = 0$ . We used Agilent Carry 5999 UV-Vis NIR Spectrophotometer to carry out the measurements.

## **Photoluminescence (PL) spectroscopy**

This is a non-destructive non-contact technique where photons stimulates the emission of a photon form a sample. Put simply, photo excitation occurs during this process causing the material to jump to a higher electronic state, releasing energy as it returns to its lower energy level. The emission of light during this process, is known as photoluminescence. For our ZnO samples PL is measured at room temperature. The measurements were performed by pumping with the 325 nm (3.82 eV) line of a He-Cd laser chopped through an acoustooptic modulator at a frequency of 55 Hz and a fixed power of 1.5 mW. The PL signal was analyzed by a single grating monochromator, detected with a Hamamatsu visible photomultiplier, and recorded with a lock-in amplifier using the acoustooptic modulator frequency as a reference.

## **EPR**

Is a distinct technique allowing the study of free radicals and paramagnetic compounds, offering an atomistic insight into the properties of a sample. As EPR spectroscopy is limited to species magnetic moment, it is combined with other spectroscopic techniques providing a

comprehensive knowledge of a sample at hand. When an external magnetic field is applied, and Zeeman splitting occurs and the resonance condition is fulfilled; here the following condition holds:

$$g_e = \frac{h \nu}{\beta_e B_0} \quad 2$$

$g_e$  represents the electron g factor, a dimensionless quantity characterizing the magnetic moment and angular momentum of an atom, particle or nucleus.

$\beta_e = 9.274 \times 10^{-24} \text{ J.T}^{-1}$  The Bohr Magnetron

$h$  = Planck's constant

$\nu$  = the frequency of the electromagnetic radiation

$B_0$  = the magnetic field applied

For a free electron g-factor is a of highly precise scalar quantity 2.0023 . But for a particular species, the anisotropy of the sample provides an average measure of g factor giving information on the symmetry of the electronic distribution for that paramagnetic species. In this thesis, we will measure and study it for ZnO samples with different morphologies. So the g value obtained is dependent on many conditions such as the molecular environment and electronic ground state, which reveals valuable chemical information. For further reading, a study summarizing of the detailed works, background and concepts by Maxie et al. gives a deep insight <sup>57</sup>. The EPR measurements in this thesis, were performed with a Bruker Benchtop EMX Nano EPR spectrometer with an integrated referencing for g-factor calculation and integrated spin counting unit. The microwave frequency of the resonator was 9.41 GHz and all spectra were measured with 5 mW microwave power at room temperature.

## 4. RESULTS AND DISCUSSION

### 4.1 X-ray Diffraction Analysis (XRD)

XRD was carried out to analyse the three different nanostructures and the lattice plane and their characteristic peaks. The particle size of each of the crystal was calculated using the Scherrer's equation:

$$D = \frac{K \lambda}{\beta \cos \theta} \quad 3$$

Where,

$D$  = Average dimension of the crystallites

$K$  = The Scherer constant

$\lambda$  = Wavelength of the X-rays

$\beta$  = FWHM in radians.

The estimated particle size of them are shown in Table 1.

**Table 1:** The estimated size of each nanomorphology obtained from Sherrer's equation.

Morphology	Particle Size
Nanoparticle	10.4 nm
Nanourchin	17.2 nm
Nanoflower	22.4 nm

Figure 12 a. is the X-ray diffraction (XRD) spectra of the three different morphologies namely, Nanoflowers (NF), Nanourchins (NU), and Nanoparticles (NP), all of which belong to the hexagonal wurtzite crystal structure formation<sup>58</sup>. Characteristic peaks are obtained at (100), (002), (101) diffraction patterns with proximate intensities for each

nanostructure. There is a shift observed in NF when compared to the other two morphologies. NF grow with unidirectional (c-axis) orientation with a 1D nanostructure.

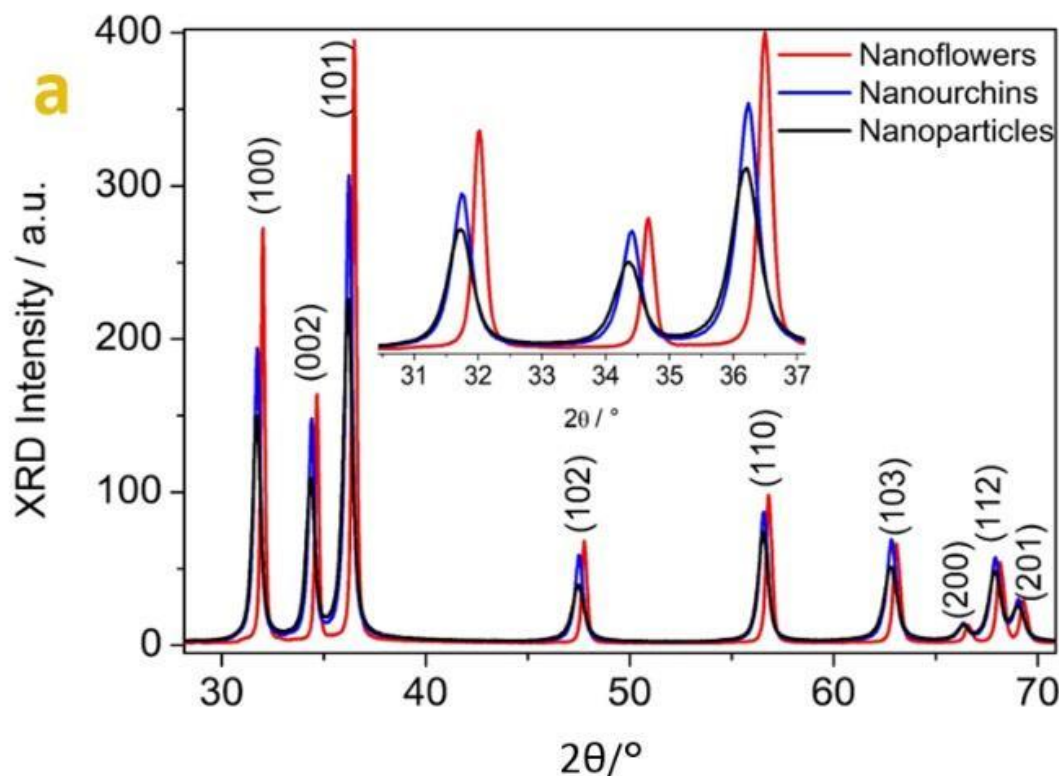


**Figure 12.** Powder X-ray diffraction patterns of ZnO nanostructures. All the indexed peaks in the obtained spectra are matched with the planes of the ZnO hexagonal wurtzite structure (01-079-0207)

When observed by SEM, a difference is noticed from the expected, the nanostructures gather to form bunches displaying a loss in their 1D preference. Accordingly the peak at (002) is not as strong at 34.72° as would be expected in a typical NF nanostructure<sup>59, 60</sup>. Also, another difference that does occur in NF is the visible shift in the XRD towards the right. The position of the diffraction peaks reveals information about the lattice planes and their location in the crystal structure. There are several reasons believed to have been the cause of the shift of NF towards the higher angles in XRD. The first common reason being there is a change in stress of the ZnO nanostructures<sup>61</sup>. The main causes of stress are that are reported in the literature are:

1. Intrinsic stress caused by defects and impurities in the crystal structure

## 2. Extrinsic stress caused by different growth conditions and lattice mismatch <sup>56, 61</sup>

Some of the reasons causing ZnO nanostructures to have stress are lattice disorders, oxygen vacancies, and zinc interstitials are among several defects that can be listed for ZnO nanostructures causing stress within the crystal structure. According to Bragg's Law, wurtzite peaks of NFs that appear at higher diffraction angles can be correlated with smaller lattice spacing within the nanostructures. The X-ray peak shift towards higher diffraction angles is brought about by a decrease in lattice spacing that can be correlated to oxygen vacancies. <sup>56</sup> Similarly, in NP and NU the presence of Zinc interstitials may result in a larger lattice spacing, causing a shift of the wurtzite diffraction peaks towards lower  $2\theta$  values. These results will be substantiated by EPR and PL analyses. It can be evaluated that the variations in the defect densities and feature sizes have created an ultimate impact in the XRD results obtained for each of these three nanostructures.

## 4.2 SEM

SEM, reveals information about the texture of the surfaces, necessary to make comparisons for each of the crystal structure in question. In Figure 13, we can visualize the texture of each morphology. Each of them is distinct from the other. It is difficult to precisely comment on their dimensions as the SEM pictures of nanoflowers and nanourchins are difficult to define.

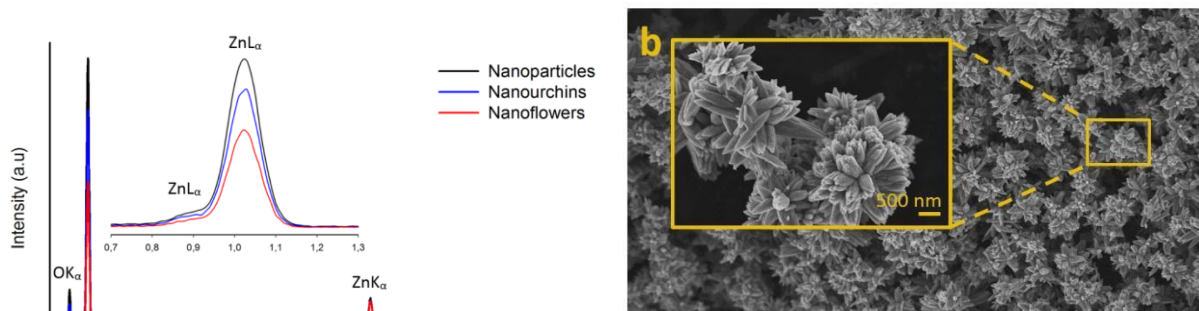


**Figure 13.** Structural and morphological investigation of different ZnO nanostructures. a) EDS spectra of three different nanostructures. The analyses were conducted at 18keV accelerating voltage. b) Secondary-electron SEM micrograph of ZnO nanoflowers, c) Secondary-electron SEM micrograph of ZnO nanourchins, and d) Secondary-electron SEM micrograph of ZnO nanoparticles. All images were recorded through an in-lens detector with an accelerating voltage of 5 keV. In the inset, higher magnification of each image is given.

However, throughout the structure each structure has displayed a reasonable homogeneity. EDS spectra also substantiates our analysis displaying a reasonable homogeneity. EDS revealed exact stoichiometry and correct atomic ratio for the ZnO crystal structure sampled.

### 4.3 Raman Spectroscopy

Raman spectroscopy enabled differentiating the phase variants and existing defect density related vibration modes of ZnO nanostructures at the molecular level. ZnO crystallizes as hexagonal wurtzite which belongs to the  $C_{6v}^4(P6_3mc)$  space group and the only optical phonons at the  $\Gamma$  point of the Brillouin zone give rise to a first order Raman scattering<sup>59, 62,</sup>

<sup>63</sup>.

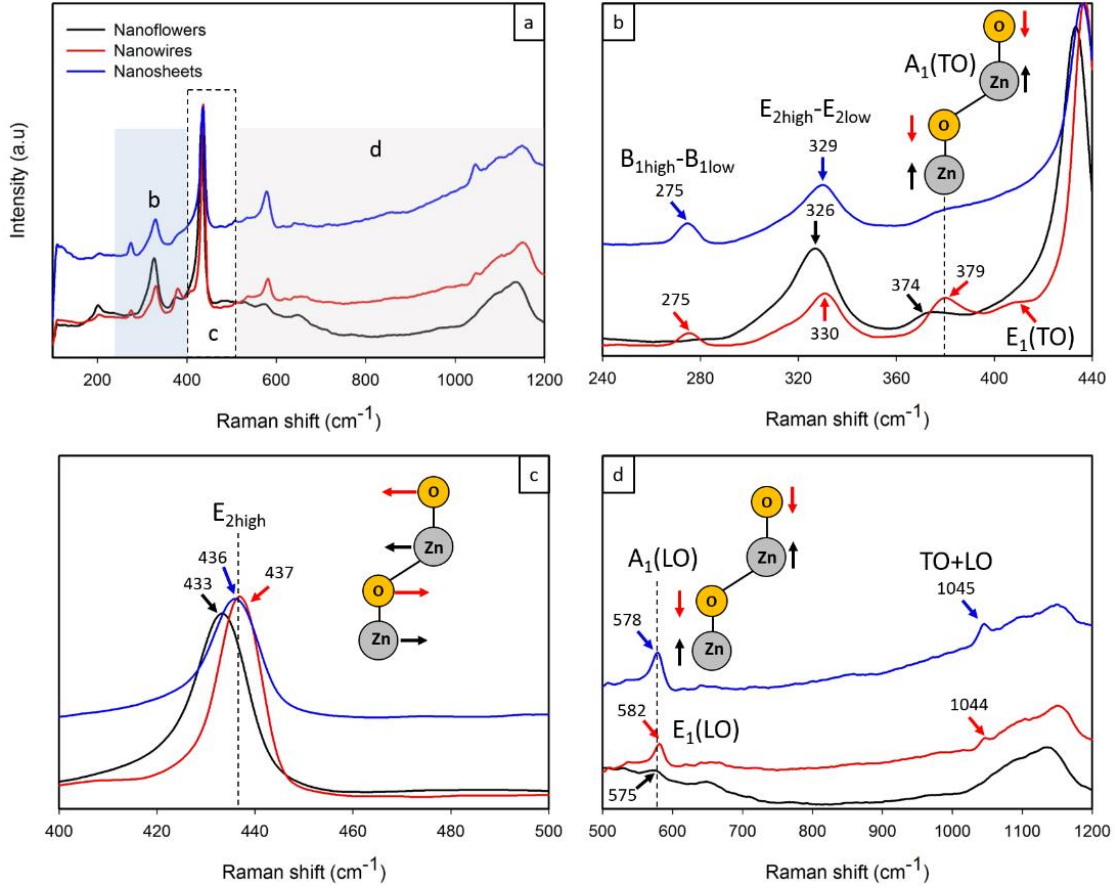


**Figure 14.** First order and second order Raman spectra of three different ZnO nanostructures ( $\lambda=532\text{nm}$ ).

The predicted zone-center optical modes are  $A_1$ ,  $2B_1$ ,  $E_1$ ,  $2E_2$  where B modes are silent<sup>63, 64</sup>. In the wurtzite structure, each Zn ion is surrounded by the tetrahedron of oxygen ions and vice versa and this orientation cause polar symmetry along the hexagonal vertical axis (c-axis) which results in  $A_1$  and  $B_1$  mode oscillations<sup>62</sup>. On the other hand, when atom displacement is perpendicular to the c-axis the twofold degenerate E modes occur. The  $E_1$  mode exhibits an oscillating polarization while  $E_2$  modes that consist of  $E_2$  (low) and  $E_2$  (high) mode mainly comes from the vibration of the O sublattice<sup>62, 64</sup>. The polarity induces a splitting of the  $A_1$  and  $E_1$  modes into transverse optical (TO) and longitudinal optical (LO) phonons.

The Raman spectra of three different ZnO nanostructures given in Figure 14(a-d), reveals the differences as a function of different morphologies. Owing to the strong presence of  $E_2$  modes in standard backscattering experiments, these modes considered to be a Raman fingerprint

for ZnO. In Figure 14(b) and (c), a strong peak at around  $436\text{ cm}^{-1}$  is assigned to the characteristic wurtzite  $E_{2\text{high}}$  mode of ZnO. This peak is shifted to lower wavenumbers in the case of NPs. Such an occurrence may be due to anisotropic internal strains corresponding to different growth directions, the defects or impurities in the nanocrystal, laser irradiation-induced heating or optical phonon confinement in different nanostructures. As the dimensions of nanostructures are bigger than the Bohr exciton radii ( $\approx 2.34\text{ nm}$ ), the optical confinement is possible but is not the only expected mechanism that occurs<sup>64</sup>. The possible effect of laser irradiation on the vibrational modes was tested by applying various laser powers. No apparent band shift or broadening was observed, allowing us to carry out the rest of the experiments at 100% laser power in the static scan. The  $E_{2(\text{low})}$  mode could not be detected for all three nanostructures (Figure 14). However, the vibration at around  $330\text{ cm}^{-1}$  is generally attributed to the second-order Raman process and assigned to the  $E_{2(\text{high})}$ - $E_{2(\text{low})}$  difference mode. This assignment is confirmed by both symmetry considerations and temperature-dependent intensity analysis<sup>62,65</sup>. Therefore, it can be concluded that  $E_{2(\text{low})}$  band may exist as broad band with low intensity. It should be considered that in the case of the second-order Raman process, predominant combination bands are present which belongs to the total frequencies of optical branches. This can be attributed to the possible surface and/or aggregate defects in the structure. This is also another indication for the existence of the structural defects. When the incident light and scattered light are perpendicular to the c-axis, TO modes were not observed for NUs. In the case of NFs, the obvious peak at  $379\text{ cm}^{-1}$  is attributed to  $A_1(\text{TO})$  mode, while the weak shoulder peak at  $408\text{ cm}^{-1}$  is assigned to  $E_1(\text{TO})$  mode. For NPs, only  $A_1(\text{TO})$  mode was observed at  $374\text{ cm}^{-1}$ . The  $A_1(\text{LO})$  phonon mode can appear only when the c-axis of the wurtzite ZnO is perpendicular to the sample surface, the  $E_1(\text{LO})$  phonon is observed at  $582\text{ cm}^{-1}$  in the case of NF (Figure 14 d). In the high frequency range, the most significant second-order features correspond to LO overtones and the combinations of LO modes<sup>65</sup>. In Figure 14 d, the broad bands, in between  $1030\text{-}1200\text{ cm}^{-1}$  should belong to the multiphonon process. The broad peak at around,  $1150\text{ cm}^{-1}$  may correspond to 2LO scattering from flat bands along the A-L-M line, possibly in combination with the modes  $2A_1(\text{LO})$  and  $2E_1(\text{LO})$  inside of the first Brillouin zone<sup>65</sup>. This band was observed was observed at  $1135\text{ cm}^{-1}$  in the case of NPs. The weak shoulders at around  $1044$

$\text{cm}^{-1}$  can be attributed to the TO+LO combinations at the A and H points of the NFs and NUs, whereas this multiphonon band could not be observed for the NPs.

**Table 3.** Room temperature frequencies and symmetries of the first-order and second-order Raman spectra observed in different ZnO nanostructures. Parentheses indicate symmetries that although being present in the spectra display a much lower intensity than the dominant one.

		Nanoparticles	Nanoflowers	Nanourchins
Symmetry	Process	Raman shift ( $\text{cm}^{-1}$ )		
A <sub>1</sub> , E <sub>2</sub>	*2TA; 2E <sub>2low</sub>	201	203	204
A <sub>1</sub>	B <sub>1high</sub> - B <sub>1low</sub>	-	275	275

A <sub>1</sub> ,(E <sub>2</sub> ,E <sub>1</sub> )	E <sub>2high</sub> - E <sub>2low</sub>	326	330	329
A <sub>1</sub>	A <sub>1</sub> (TO)	374	379	-
E <sub>1</sub>	E <sub>1</sub> (TO)	-	408	-
E <sub>2</sub>	E <sub>2high</sub>	433	437	436
A <sub>1</sub>	A <sub>1</sub> (LO)	575	-	578
E <sub>1</sub>	E <sub>1</sub> (LO)	-	581	-
A <sub>1</sub>	**TO+LO	-	1044	1045
A <sub>1</sub>	***2A <sub>1</sub> (LO),2E <sub>1</sub> (LO); 2LO	1135	1154	1151

\*L,M,H;  $\Gamma$  Brillouin zone points/lines <sup>62, 65</sup>, \*\*A, H Brillouin zone points/lines <sup>62, 65</sup>, \*\*\*  $\Gamma$ ; A-L-M Brillouin zone points/lines <sup>62, 65</sup>.

#### 4.4 Photoluminescence Spectroscopy

Photoluminescence Spectroscopy is sensitive to all types of defect. However, in EPR spectroscopy, which will be inspected later on, is only sensitive to paramagnetic defects but by the aid of EPR, it is possible to distinguish surface and core defects due to the g-factor difference. Namely, the point defects located at the surface give  $g \sim 2$  and at the core gives  $\sim 1.96$  <sup>66</sup>. Therefore, it is crucial to determine defect art from PL, and their location form EPR <sup>67</sup>.

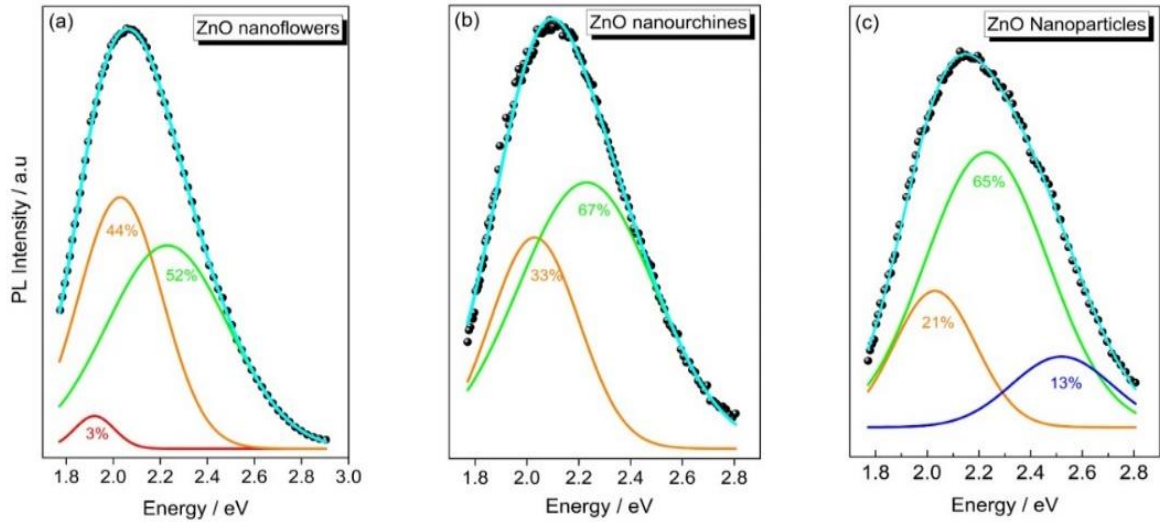


**Figure 15.** The PL intensity versus energy graphs (a-c) for the different ZnO nanostructures.

**Table 4.** Provides a summary of the result obtained from the PL graphs.

		Nanoflowers	Nanoparticles	Nanourchins
$V_{Zn}$	Blue	-	13%	-
$V_{O^+}$	Green	53%	65%	67%
$V_O$	Orange	44%	21%	33%
$O_i$	Red	3%	-	-

In Figure 15 (a-c) it is observed, three PL spectra for different morphologies of ZnO. Defect related PL spectra originate from all kinds of defects in ZnO and the green emission is mostly responsible for the  $V_o$ .

According to PL, blue (13% for NF), green (65%, 67%, and 52% for NPs, NUs, and NF, respectively) orange (33% and 44% for NU and NF) and finally red emission (3%) is related to Zn vacancies ( $V_{Zn}$ ) at the surface, singly ionized oxygen vacancies ( $V_o^+$ ) at the surface, oxygen vacancies ( $V_o$ ) at the core and to the interstitial oxygen ( $O_i$ ) located at the surface respectively <sup>68</sup>. From these results, we confirm that the defect structures are strongly dependent on the morphology. There is a strong tendency of redshift in NF even red emission is observed indicating  $O_i$  defects. From the EPR point of view, all paramagnetically active defect centers have been already listed in our previous works. <sup>66, 67, 69</sup>

#### 4.5 UV-Vis Spectroscopy

The band gap energy of the various morphologies of ZnO samples were measured using reflection spectra that were performed via UV-Vis spectroscopy

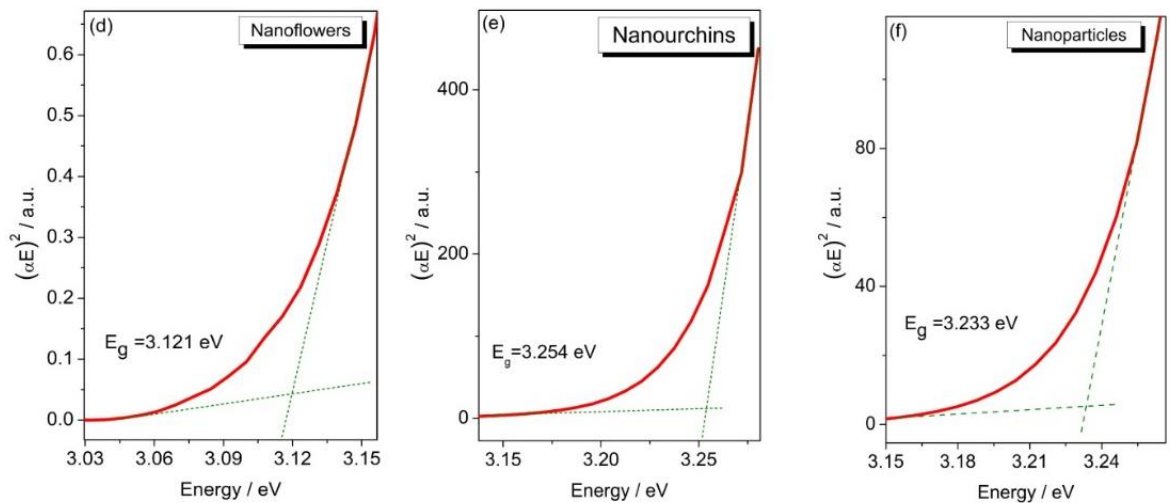


**Figure 16.** Tauc-plots (d-f) obtained from UV-Vis reflectance spectra for the different ZnO nanostructures.

For determining the bandgap experimentally, the absorption coefficient  $\alpha$  is deduced from the following equation:

$$\alpha = \ln \left[ \frac{R_{max} - R_{min}}{R - R_{min}} \right] \quad 4$$

Where,

$R$  = Reflectance value

$R_{max}$  = Maximum Reflectance value

$R_{min}$  = Minimum Reflectance value

$\alpha$  = Absorption co-efficient

Then in this approximated technique typically a curve between  $(\alpha h\nu)^2$  versus photon energy ( $h\nu$ ) is plotted. The intercept of this plot on the energy axis is defined as the bandgap of ZnO nanocrystals. This procedure is commonly used for determining the bandgap energy of semiconductors<sup>70, 71</sup>. By the examination of bandgap energies by UV–Vis spectroscopy following bandgap energy ( $E_g$ ) values was obtained by the aid of Tauc-plot as presented in Figure 16 (d-f): 3.233 eV, 3.121 eV, and 3.254 eV for nanoparticles, nanoflowers and nanourchins, respectively. Certainly, this method gives approximately the accurate estimation of bandgap however it may not be reliable enough to correlate the  $E_g$  values with defect concentration or any other physical parameters such as conductivity, capacitance, or g-factor.

#### **4.6 EPR Spectroscopy**

The EPR Figure 17a, shows two distinct EPR signal at  $g=2.002$  and  $g=1.962$ . As previously discussed, the signal at  $g=2.002$  is arising from the defect centers in ZnO located at the surface and  $g=1.962$  signal is arising from the defects located at the core of the ZnO. Here, in combination with PL we not only have tested the morphology dependence of defect centers in ZnO but also their concentration dependency by the aid of spin counting procedure<sup>72, 73</sup>.

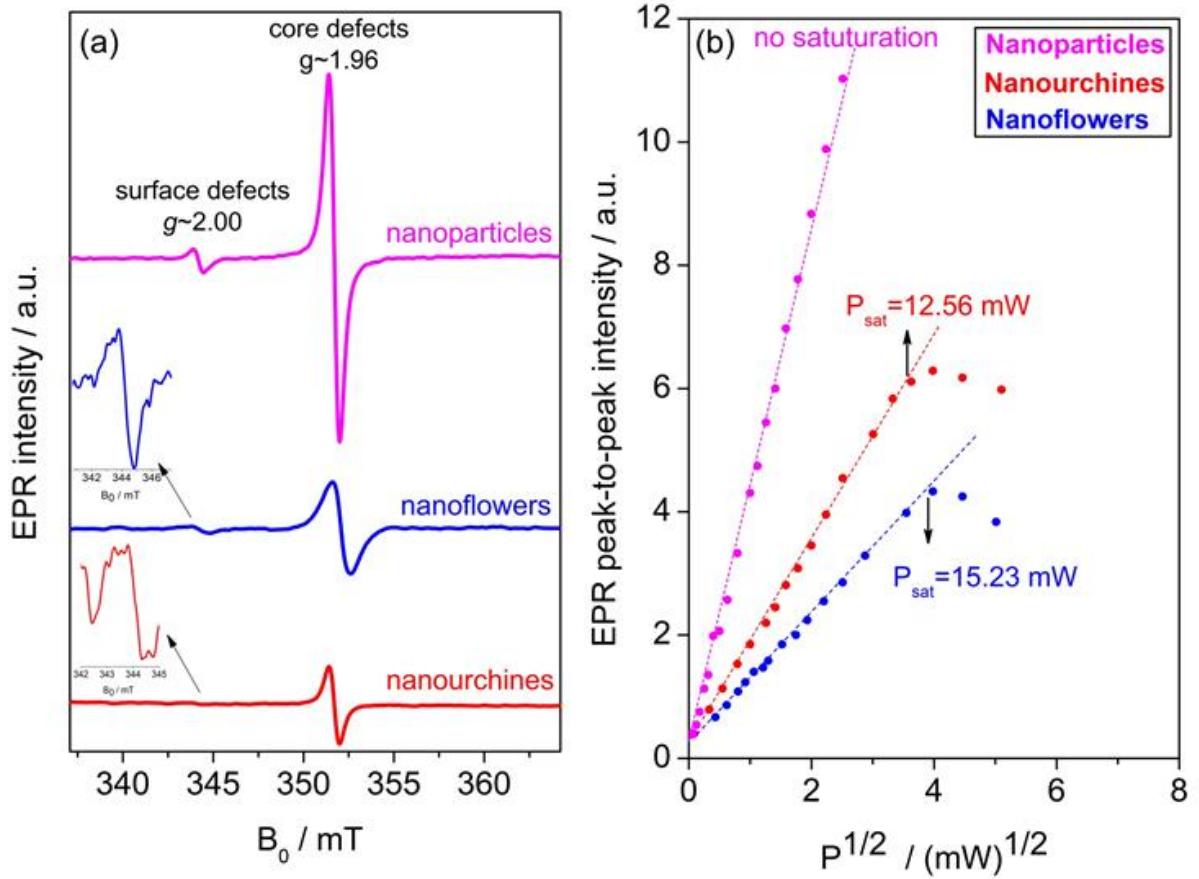


**Figure 17.** (a) Intensity measured at room temperature X band (9.47Hz) EPR and (b) plot of EPR peak to peak intensity with respect to  $P^{1/2}$  for the hydrothermal processed three different nanostructures of ZnO.

**Table 5.** Different recorded parameters for core and shell of the various ZnO nanostructures.

	<b>g-factor</b>	<b>Defect concentration (spins/mg)</b>	<b>Power saturation (mW)</b>
<b>Nanoparticles</b>			
<i>Core</i>	1.9591	$2.23 \times 10^{13}$	No saturation
<i>Shell</i>	2.0027	$7.65 \times 10^{11}$	-
<b>Nanoflowers</b>			
<i>Core</i>	1.9580	$3.56 \times 10^{12}$	15.23
<i>Shell</i>	2.0024	$2.45 \times 10^{11}$	-
<b>Nanourchins</b>			
<i>Core</i>	1.9597	$0.56 \times 10^{12}$	12.56
<i>Shell</i>	2.0034	$0.12 \times 10^{11}$	-

Moreover, by the aid of EPR it is possible to determine the saturation behavior of the defect centers which give rise to EPR signal meaning that the ones which are paramagnetic. Microwave saturation data, in general, give <sup>1</sup> information on the trap electrons whether they are bounded or unbounded. Further one may obtain information about the spin-lattice relaxation time <sup>74, 75</sup>. As it is seen from Figure 17 a, all three nano-morphology (particles, urchin, and flower) have core signals. On the other hand, the EPR intensity of shell signal hence the concentration of surface defects is strongly dependent on the morphology. From the extended figures, it is seen that NUs have decreased concentration of surface defects. NPs have the highest number of defects compared to NF and NU. It is known that the conduction electrons saturate easily<sup>32, 66, 69, 72</sup>, whereas the bound-state electrons saturate with much more difficulty with respect to the square root of microwave power. Therefore, according to our past research on defects in the frame of the core-shell model that one expects easy saturation for surface defects and hard or almost no saturation for core defects. This has been already proved by the investigation of various ZnO monocrystalline samples <sup>67, 69, 72</sup> and also for

carbon materials such as C-dots<sup>33</sup>. In present work, we realized that the defect structure thus the behavior of them under microwave power is completely different and quite complicated. Since the EPR signal of surface defects around  $g\sim 2$  is too weak so that we cannot perform reliable power dependency on this signal for all three samples. Based on the power dependency of the core defects at  $g\sim 1.96$  we may say that the nanoparticles follow the expectation of the core-shell model where there is no saturation in the EPR intensity. However, according to electrical results (will be given below), this sample has the highest conductivity. That means the defect type change from  $V_o$  to either  $V_{Zn}$  or  $O_i$ . While in ZnO particles the major defect center is expected to be the  $V_o$  due to their lower formation energy. Thus, here the situation changed and this is most probably based on the synthesis route. As listed in Table 2, in the case of nanoflowers and nanourchins strong saturation behavior is observed at 15.23 mW and 12.56 mW, respectively. This means the core defects are acting as surface defects. This sounds strange however the morphology of the ZnO changed the electronic environment thereby the local configuration and the saturated core defects are revealed, unexpectedly. This also means that morphology dependent defect centers may drastically alter the spin-lattice relaxation times.

## 5. SUPERCAPACITOR DEVICE TEST

### 5.1 Electrical Impedance Spectroscopy

Electrical impedance spectroscopy (EIS) measurements were carried out using a Versastat IV potentiostat (Princeton Applied Research) in atmospheric pressure at room temperature in the frequency range between 0.1 Hz and 100 kHz. For analyzing the spectra we used the Versa Studio V2.4 software.

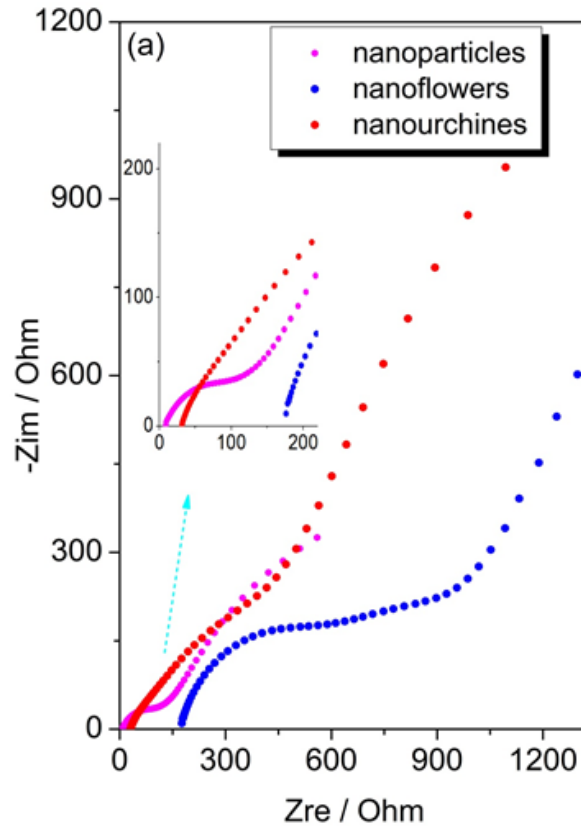


**Figure 18.** The electrochemical behavior of three produced supercapacitors investigated by EIS in Nyquist plot of the supercapacitors.

Normally, ZnO material shows resistance values in the order of Giga-Ohm<sup>72</sup>, here due to the synergy of ZnO, electrolyte, and the carbon black the supercapacitor revealed resistance values in order of approx. 50-1000 Ohm depending on the morphology of the ZnO material. In Nyquist data, the first semicircle is responsible for the charge transfer resistance  $R_{ct}$  which is the lowest for nanoparticles (less than 100  $\Omega$ ). Compared to nanoparticles the nanoflowers and nanourchins which are less defective than the nanoparticles revealed higher  $R_{ct}$ . It is

worth mentioning that faradaic storage mechanisms, in general, show higher conductivity which also confirmed here by Nyquist in the case of nanoparticles. This is quite good agreement with the EPR microwave power saturation data as well which is presented in Figure 17b. On the other hand, nanourchins show some traces of the ideal supercapacitor due to the non-existing first semicircle.

## 5.2 Cyclic Voltammetry

For all supercapacitors, cyclic voltammetry (CV) was performed in voltage ranges of -1 V to 1 V for the cells with  $\text{LiPF}_6$  electrolyte with the voltage sweeping rate of  $0.01 \text{ V s}^{-1}$ . In the present case, a four-point electrode-setup was used to measure the real supercapacitor devices.

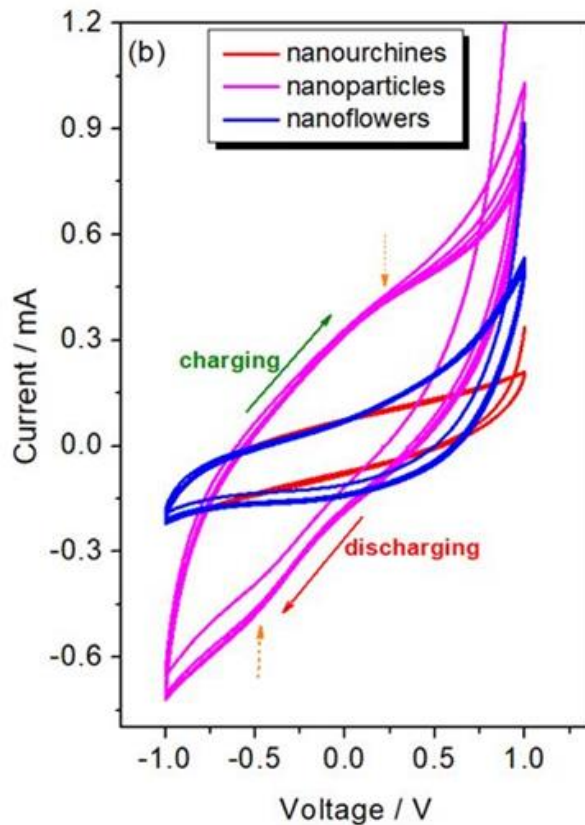


**Figure 19.** Investigation by behavior of charge-discharge (intercalation-deintercalation) via the cyclic voltammetry (CV) for observing the electrochemical behavior of three produced supercapacitors.

For less defective samples the CV curve should give curves like rectangular shape and the nanoparticles which are almost Faradaic should reveal deviated rectangular form by humps. This has been tested via potentiostat and results are presented in Figure 19 b. CV plots for each device based on morphologically different ZnO electrodes display quasi-rectangular shapes, the CV curves became leaf-like and mirror-symmetric in shape. The curves are indicating modest ideal supercapacitive properties and outstanding reversibility of the electrodes. Each device has an almost similar nature which indicates that each device can perform within potential window -1 to 1 V without any degradation. This result also indicates the dominance of the electrical double layer mechanism in the energy storage process. Normally, when ZnO is used as highly defective material as the electrode, then the pseudocapacitance behavior is expected. This has been confirmed by our previous supercapacitor studies as well.

From the defect point of view, concentrations compare to other synthesis techniques present synthesis route revealed several orders of less defect centers in all morphologies compared to superbats<sup>30</sup>, or high energy ball milled ZnO nanocrystals<sup>34</sup>. From the EPR spin counting data, this has been confirmed and given in Table 2. In particular, the decrease in surface defects from nanoparticles, nanoflowers, and nanourchins, respectively can be correlated to not only capacitive behavior but also storage mechanism. Nevertheless, CV curve of nanoparticles given in Figure 19 b has slightly deviated from the quasi-rectangular shape and showed small humps indicating Faradaic reaction. The orange dashed arrows indicate the humps for eyes in the Figure 19 b. That means in case nanoparticles has sufficient defect centers both on bulk and surface such bumps will be rising and create extra room for charges to give high capacitance values. Such a result, compare to other highly defective ZnO electrodes, shows that the morphology thus the concentration, and the synthesis route are playing crucial role for the capacitive performance of the supercapacitor devices. More than this, the defect concentration determines the working principle of the device whether it is EDLC or pseudocapacitance. Therefore, by defect mediated supercapacitors it may be possible to control the energy storage mechanism. Further, The gravimetric ( $C, F \cdot g^{-1}$ ) specific capacitance can be obtained from these CV curves at certain current density based on the following equation:  $C = I / m (\Delta V / \Delta t)$  where  $I$  (A) is the discharge current,  $\Delta t$  (s) is the discharge time,  $m$  (g) is the mass of active materials (the areal density of ZnO and carbon

black on the electrode is ca.  $20 \text{ mg}\cdot\text{cm}^{-2}$ ) and  $\Delta V$  (V) is the operation discharge voltage window. Finally, the calculated specific capacitance values are 330 F/g, 177 F/g, and 66 F/g at 0.1 C current density for nanoparticles, nanoflowers, and nanourchins, respectively. These capacitance values are lower than the pseudocapacitive superbat device which is based on a highly defective ZnO electrode that is yielding 448 F/g specific capacitance. The decrease in capacitance can be associated to the low utilization of electroactive materials at lower defect concentrations since the limited amount of electrolyte ions can enter into the inner structure and outer active surface of the active material. In the case of defective ZnO the scenario is much different. Due to the high amount of defect concentration blocking mechanisms of electron transport occurs at the interfaces and organizes as a double layer and contribute to the capacitance. These make extra room (like a camel-hump) for point charges and increase the capacitive behavior. In other words; the number of mobile defects transporting absorbed within the medium could be higher with enhanced mobility which helps in improving the charge storage capacitive behavior. Lower defect concentration blocks the ion migration within the electrolyte and diminishes the charge accumulation at the electrolyte-electrode interface. Therefore, fewer defects are drifted from an electrode to another electrode and hence less absorbed onto the active electrode forming charge accumulation at the electrode-electrolyte region.

## 6. CONCLUSIONS

In this thesis, almost all types of supercapacitors are chosen to be analyzed in terms of their electrode materials, their designs, electrolyte. This provides a connection to the specific capacitance values provided with the working principles of each type of supercapacitor along with nuances at the nanoscale that lead to their inherent structural and mechanical properties. To complete the portrayal in each category, favoured traits of high energy density, power density, high adsorption, compressibility was balanced with imperfections or defects and challenges like that of poor porosity, low conductivity, imbalance at redox sites, degradation, rise in internal resistance, increase in equivalent series resistance etc. The mechanism of storage principles along with the categorization of supercapacitors has been summarized within this thesis. The need for all kinds of supercapacitors can be justified due to the limitations of present energy harvesting and storage devices. It is obvious that each type of supercapacitors finds their applications their demand and their technological improvement. Especially, the applications of the pseudo and hybrid supercapacitors are on the growth particularly in the field of electric vehicles while most of the power consumption of the vehicles can be supplied by high-power supercapacitor devices. The ultimate goal in supercapacitor or ultracapacitor both in research and industry is to obtain high power density and high energy density altogether. This difficult task can be obtained not only by the highly tailored design of the capacitors but also through the development of electrodes, electrolytes and separator materials. Electrochemical performance test techniques also play a crucial role to investigate the device itself. Of course, this requires further fundamental understanding of both experimental and theoretical investigations. For the synthesis, design and optimization of new electrodes, smaller sizing of electrodes down to sub-nanometers, electrical and ionic conductivity, mechanical and thermal stability, a better fundamental understanding by both theoretical and experimental work is highly required. It is crucial to fundamentally understand the working principles of electrode materials, and the charge-discharge (intercalation-deintercalation) process in more realistic supercapacitor designs. Technological developments on instrumentation together with materials science and engineering enables scientists and engineers in the near future to produce next-generation robust high power capacitors which may be used as alternative energy storage and harvesting system for electrical mobile systems such as electrical vehicles, space solar panels and wind tribunes.

Various types of ZnO nanoscaled morphologies were synthesized here successfully and characterized via the XRD, SEM, and EDS from the structural point of view. Point defects for each morphology have been identified and quantitatively analyzed via Raman, PL and in particular with EPR. The detailed EPR analysis such as spin counting and microwave power saturation revealed extensive information on the local electronic environment, concentration, and location of the defect centers. According to the results, the defect centers play a central role for defect-related emission which arise from all defects exists in the ZnO sample. On the other hand, paramagnetic defects mostly singly or doubly ionized vacancies or interstitials can only be detected via EPR spectroscopy solely. The surface and core defects can be separated safely due to their *g*-factor and here NP, NF, and NU samples compared to other nanostructured samples in literature the surface defect concentration is too less. Moreover, in these specific samples, the defects on the core do not properly follow the core-shell model. The defect centers behave like a surface defect indicating conductive behavior. This can only be explained by the character of the synthesis technique and the morphology. The core-shell model has been proposed by the well-defined hexagonal nanocrystals whereas here we have quite different structures having an undefined aspect ratio. Real supercapacitor devices assembled for understanding the capacitive behavior of ZnO nano-morphologies. Here the synergy of the ZnO with the electrolyte and the counter electrode carbon black played a vital role in the electrochemical performance. Normally defective metal oxides reveal Faradaic storage mechanism once they are used as an electrode in supercapacitors. Surprisingly, we obtained EDLC character in the supercapacitor devices particularly for the less defective nanourchin samples. When the defects increase then the CV curve revealed humps which are an indication of Faradaic reaction. These results suggest that by the aid of defect centers and the morphology it is possible to predict the storage mechanism of the supercapacitor devices. This might be the first time that the defects, morphology, and the synergy of electrodes collectively show a control mechanism for EDLC and pseudosupercapacitor character. Such an interesting result should be further confirmed for other nanostructured ZnO morphologies such as nanodiscs, nanotetrapods, nanostars, nanoplates etc.

## **7. FUTURE WORKS**

The next milestone is to study to build prototypes that will make it a viable option as a device and what it takes to build one. This is a necessary shift that to build samples that endure extreme conditions and also, standing the test of time. It is a more demanding path but a necessary one to curb consumption and support a system that will mitigate the externalities that society and the environment dearly pays.

This has been the first stepping-stone of what our future projects will uphold. We conducted a comparative study of the role of three different ZnO morphologies Nanoflowers, nanourchins and nanoparticles on the supercapacitor performance. The next prospect would be to explore the effects of the carbon black as an electrode material and the choice of electrolyte. Another aspect that will provide a deeper look behind the device is the 'point of failure' of the device. The mechanisms that are otherwise left unexplored in the long lifetime of the device also would allow device performance to be enhanced.

Overall, this has been a comparative study and this should be confirmed in other nanomorphologies and more importantly taking a path using ab-initio (from scratch) methods to a final product, which would mean scrapping out the options that are not viable.

## 8. REFERENCES

- 1 S. Najib and E. Erdem, "Current progress achieved in novel materials for supercapacitor electrodes: mini review," *Nanoscale Advances*, vol. 1, no. 8, pp. 2817-2827, 2019.
- 2 N. J. J. de Klerk, E. van der Maas, and M. Wagemaker, "Analysis of Diffusion in Solid-State Electrolytes through MD Simulations, Improvement of the Li-Ion Conductivity in  $\beta$ -Li3PS4 as an Example," *ACS Applied Energy Materials*, vol. 1, no. 7, pp. 3230-3242, 2018,.
- 3 S. J. Kwon, T. Kim, B. M. Jung, S. B. Lee, and U. H. Choi, "Multifunctional Epoxy-Based Solid Polymer Electrolytes for Solid-State Supercapacitors," *ACS Applied Materials & Interfaces*, vol. 10, no. 41, pp. 35108-35117, 2018.
- 4 B. Anothumakkool, A. Torris A. T, S. Veeliyath, V. Vijayakumar, M. V. Badiger, and S. Kurungot, "High-Performance Flexible Solid-State Supercapacitor with an Extended Nanoregime Interface through in Situ Polymer Electrolyte Generation," *ACS Applied Materials & Interfaces*, vol. 8, no. 2, pp. 1233-1241, 2016.
- 5 H. Sun, Z. Xu, and C. Gao, "Multifunctional, Ultra-Flyweight, Synergistically Assembled Carbon Aerogels," *Advanced Materials*, vol. 25, no. 18, pp. 2554-2560, 2013.
- 6 T. F. B. Marcus A Worsley, "Carbon Aerogels ", 2016.
- 7 Y. Hu *et al.*, "Superelastic Carbon Aerogel with Ultrahigh and Wide-Range Linear Sensitivity," *ACS Applied Materials & Interfaces*, vol. 10, no. 47, pp. 40641-40650, 2018.
- 8 C. Moreno-Castilla and F. J. Maldonado-Hódar, "Carbon aerogels for catalysis applications: An overview," *Carbon*, vol. 43, no. 3, pp. 455-465, 2005.
- 9 Q. Ke and J. Wang, "Graphene-based materials for supercapacitor electrodes – A review," *Journal of Materiomics*, vol. 2, no. 1, pp. 37-54, 2016.
- 10 J. N. Coleman, U. Khan, W. J. Blau, and Y. K. Gun'ko, "Small but strong: A review of the mechanical properties of carbon nanotube–polymer composites," *Carbon*, vol. 44, no. 9, pp. 1624-1652, 2006.
- 11 Y. Jang, J. Jo, H. Jang, I. Kim, D. Kang, and K.-Y. Kim, "Activated carbon/manganese dioxide hybrid electrodes for high performance thin film supercapacitors," *Applied Physics Letters*, vol. 104, no. 24, p. 243901, 2014.
- 12 N. Shimodaira and A. Masui, "Raman spectroscopic investigations of activated carbon materials," *Journal of Applied Physics*, vol. 92, no. 2, pp. 902-909, 2002.
- 13 R. Heimböckel, F. Hoffmann, and M. Fröba, "Insights into the influence of the pore size and surface area of activated carbons on the energy storage of electric double layer capacitors with a new potentially universally applicable capacitor model," *Physical Chemistry Chemical Physics*, vol. 21, no. 6, pp. 3122-3133, 2019.
- 14 J. C. E. Marin S. Halper, "Supercapacitors: A Brief Overview," *MITRE, Technical Papers*, March 2006.
- 15 C. Masarapu, L.-P. Wang, X. Li, and B. Wei, "Tailoring Electrode/Electrolyte Interfacial Properties in Flexible Supercapacitors by Applying Pressure," *Advanced Energy Materials*, vol. 2, no. 5, pp. 546-552, 2012.
- 16 D. I. Abouelamaiem *et al.*, "Synergistic relationship between the three-dimensional nanostructure and electrochemical performance in biocarbon supercapacitor electrode materials," *Sustainable Energy & Fuels*, vol. 2, no. 4, pp. 772-785, 2018.
- 17 H. Itoi, H. Hasegawa, H. Iwata, and Y. Ohzawa, "Non-polymeric hybridization of a TEMPO derivative with activated carbon for high-energy-density aqueous electrochemical capacitor electrodes," *Sustainable Energy & Fuels*, vol. 2, no. 3, pp. 558-565, 2018.

- 18 X. Ma *et al.*, "Excellent Compatibility of the Gravimetric and Areal Capacitances of an Electric-Double-Layer Capacitor Configured with S-Doped Activated Carbon," *ChemSusChem*, vol. 11, no. 21, pp. 3766-3773, 2018.
- 19 M. Vangari, T. Pryor, and L. Jiang, "Supercapacitors: Review of Materials and Fabrication Methods," *Journal of Energy Engineering*, vol. 139, no. 2, pp. 72-79, 2013.
- 20 M. D. Stoller, S. Park, Y. Zhu, J. An, and R. S. Ruoff, "Graphene-Based Ultracapacitors," *Nano Letters*, vol. 8, no. 10, pp. 3498-3502, 2008.
- 21 A. Kausar, "Overview on conducting polymer in energy storage and energy conversion system," *Journal of Macromolecular Science, Part A*, vol. 54, no. 9, pp. 640-653, 2017.
- 22 M. Y. Ho, P. S. Khiew, D. Isa, T. K. Tan, W. S. Chiu, and C. H. Chia, "A Review Of Metal Oxide Composite Electrode Materials For Electrochemical Capacitors," *Nano*, vol. 09, no. 06, p. 1430002, 2014.
- 23 A. L. M. Reddy and S. Ramaprabhu, "Nanocrystalline Metal Oxides Dispersed Multiwalled Carbon Nanotubes as Supercapacitor Electrodes," *The Journal of Physical Chemistry C*, vol. 111, no. 21, pp. 7727-7734, 2007.
- 24 H. D. Yoo *et al.*, "'Rocking-Chair'-Type Metal Hybrid Supercapacitors," *ACS Applied Materials & Interfaces*, vol. 8, no. 45, pp. 30853-30862, 2016.
- 25 H. Gao, F. Xiao, C. B. Ching, and H. Duan, "High-Performance Asymmetric Supercapacitor Based on Graphene Hydrogel and Nanostructured MnO<sub>2</sub>," *ACS Applied Materials & Interfaces*, vol. 4, no. 5, pp. 2801-2810, 2012.
- 26 M. Zhi, C. Xiang, J. Li, M. Li, and N. Wu, "Nanostructured carbon-metal oxide composite electrodes for supercapacitors: a review," *Nanoscale*, vol. 5, no. 1, pp. 72-88, 2013.
- 27 A. Ghosh *et al.*, "High Pseudocapacitance from Ultrathin V<sub>2</sub>O<sub>5</sub> Films Electrodeposited on Self-Standing Carbon-Nanofiber Paper," *Advanced Functional Materials*, vol. 21, no. 13, pp. 2541-2547, 2011.
- 28 M. Zhi, A. Manivannan, F. Meng, and N. Wu, "Highly conductive electrospun carbon nanofiber/MnO<sub>2</sub> coaxial nano-cables for high energy and power density supercapacitors," *Journal of Power Sources*, vol. 208, pp. 345-353, 2012.
- 29 D. P. Dubal, O. Ayyad, V. Ruiz, and P. Gómez-Romero, "Hybrid energy storage: the merging of battery and supercapacitor chemistries," *Chemical Society Reviews*, vol. 44, no. 7, pp. 1777-1790, 2015.
- 30 S. Kasap, I. I. Kaya, S. Repp, and E. Erdem, "Superbat: battery-like supercapacitor utilized by graphene foam and zinc oxide (ZnO) electrodes induced by structural defects," *Nanoscale Advances*, vol. 1, no. 7, pp. 2586-2597, 2019.
- 31 M. Tuncer, F. Bakan, H. Gocmez, and E. Erdem, "Capacitive behaviour of nanocrystalline octacalcium phosphate (OCP) (Ca<sub>8</sub>H<sub>2</sub>(PO<sub>4</sub>)<sub>6</sub>·5H<sub>2</sub>O) as an electrode material for supercapacitors: biosupercaps," *Nanoscale*, vol. 11, no. 39, pp. 18375-18381, 2019.
- 32 R. Genc *et al.*, "High-Capacitance Hybrid Supercapacitor Based on Multi-Colored Fluorescent Carbon-Dots," *Scientific Reports*, vol. 7, no. 1, p. 11222, 2017.
- 33 M. Alaş, A. Güngör, R. Genç, and E. Erdem, "Feeling the power: robust supercapacitors from nanostructured conductive polymers fostered with Mn(2+) and carbon dots," *Nanoscale*, vol. 11, no. 27, pp. 12804-12816, 2019.
- 34 M. Toufani, S. Kasap, A. Tufani, F. Bakan, S. Weber, and E. Erdem, "Synergy of nano-ZnO and 3D-graphene foam electrodes for asymmetric supercapacitor devices," *Nanoscale*, vol. 12, no. 24, pp. 12790-12800, 2020.
- 35 Y. Li *et al.*, "Tuning morphology and conductivity in two-step synthesis of zinc-cobalt oxide and sulfide hybrid nanoclusters as highly-performed electrodes for hybrid supercapacitors," *Journal of Solid State Electrochemistry*, vol. 22, 2018.

- 36 K. Subramani and M. Sathish, "Facile synthesis of ZnO nanoflowers/reduced graphene oxide nanocomposite using zinc hexacyanoferrate for supercapacitor applications," *Materials Letters*, vol. 236, pp. 424-427, 2019.
- 37 W. K. Chee, H. N. Lim, and N. M. Huang, "Electrochemical properties of free-standing polypyrrole/graphene oxide/zinc oxide flexible supercapacitor," *International Journal of Energy Research*, vol. 39, no. 1, pp. 111-119, 2015.
- 38 B. Pant *et al.*, "Carbon nanofibers wrapped with zinc oxide nano-flakes as promising electrode material for supercapacitors," *Journal of Colloid and Interface Science*, vol. 522, pp. 40-47, 2018.
- 39 M. S. Yadav, N. Singh, and A. Kumar, "Synthesis and characterization of zinc oxide nanoparticles and activated charcoal based nanocomposite for supercapacitor electrode application," *Journal of Materials Science: Materials in Electronics*, vol. 29, no. 8, pp. 6853-6869, 2018.
- 40 Y. Haldorai, W. Voit, and J.-J. Shim, "Nano ZnO@reduced graphene oxide composite for high performance supercapacitor: Green synthesis in supercritical fluid," *Electrochimica Acta*, vol. 120, pp. 65-72, 2014.
- 41 G. Guo *et al.*, "Sandwiched nanoarchitecture of reduced graphene oxide/ZnO nanorods/reduced graphene oxide on flexible PET substrate for supercapacitor," *Applied Physics Letters*, vol. 99, no. 8, p. 083111, 2011.
- 42 X. Xiao, B. Han, G. Chen, L. Wang, and Y. Wang, "Preparation and electrochemical performances of carbon sphere@ZnO core-shell nanocomposites for supercapacitor applications," *Scientific Reports*, vol. 7, no. 1, p. 40167, 2017.
- 43 A. Sahoo and Y. Sharma, "Synthesis and characterization of nanostructured ternary zinc manganese oxide as novel supercapacitor material," *Materials Chemistry and Physics*, vol. 149-150, pp. 721-727, 2015.
- 44 M. Saranya, R. Ramachandran, and F. Wang, "Graphene-zinc oxide (G-ZnO) nanocomposite for electrochemical supercapacitor applications," *Journal of Science: Advanced Materials and Devices*, vol. 1, no. 4, pp. 454-460, 2016.
- 45 X. Hou *et al.*, "Ultrathin ZnS nanosheet/carbon nanotube hybrid electrode for high-performance flexible all-solid-state supercapacitor," *Nano Research*, vol. 10, no. 8, pp. 2570-2583, 2017.
- 46 C. J. Raj *et al.*, "Two-Dimensional Planar Supercapacitor Based on Zinc Oxide/Manganese Oxide Core/Shell Nano-architecture," *Electrochimica Acta*, vol. 247, pp. 949-957, 2017.
- 47 K. S. Lee, C. W. Park, and J.-D. Kim, "Synthesis of ZnO/activated carbon with high surface area for supercapacitor electrodes," *Colloids and Surfaces A: Physicochemical and Engineering Aspects*, vol. 555, pp. 482-490, 2018.
- 48 C. H. Kim and B.-H. Kim, "Zinc oxide/activated carbon nanofiber composites for high-performance supercapacitor electrodes," *Journal of Power Sources*, vol. 274, pp. 512-520, 2015.
- 49 N. I. T. Ramli, S. A. Rashid, M. S. Mamat, Y. Sulaiman, S. A. Zobir, and S. Krishnan, "Incorporation of Zinc Oxide into Carbon nanotube/Graphite nanofiber as high performance supercapacitor electrode," *Electrochimica Acta*, vol. 228, pp. 259-267, 2017.
- 50 S. Yang *et al.*, "Controllable ZnFe<sub>2</sub>O<sub>4</sub>/reduced graphene oxide hybrid for high-performance supercapacitor electrode," *Electrochimica Acta*, vol. 268, pp. 20-26, 2018.
- 51 T.M.Project,"From Ab-initio Calculations."
- 52 T. M. Project, "The Zinc Oxide Wurtzite Crystal Structure."

- 53 F. S. Husairi, S. M. Ali, A. Azlinda, M. Rusop, and S. Abdullah, "Special Effect of Urea as a Stabilizer in Thermal Immersion Method to Synthesis Porous Zinc Oxide Nanostructures," *Journal of Nanomaterials*, vol. 2013, p. 163527, 2013.
- 54 K. Kakiuchi, E. Hosono, T. Kimura, H. Imai, and S. Fujihara, "Fabrication of mesoporous ZnO nanosheets from precursor templates grown in aqueous solutions," *Journal of Sol-Gel Science and Technology*, vol. 39, no. 1, pp. 63-72, 2006.
- 55 X. Wen, W. Wu, Y. Ding, and Z. L. Wang, "Seedless synthesis of patterned ZnO nanowire arrays on metal thin films (Au, Ag, Cu, Sn) and their application for flexible electromechanical sensing," *Journal of Materials Chemistry*, vol. 22, no. 19, pp. 9469-9476, 2012.
- 56 J. Ungula, B. F. Dejene, and H. C. Swart, "Effect of annealing on the structural, morphological and optical properties of Ga-doped ZnO nanoparticles by reflux precipitation method," *Results in Physics*, vol. 7, pp. 2022-2027, 2017.
- 57 M. M. Roessler and E. Salvadori, "Principles and applications of EPR spectroscopy in the chemical sciences," *Chemical Society Reviews*, vol. 47, no. 8, pp. 2534-2553, 2018.
- 58 N. Abdullayeva *et al.*, "Investigation of Strain Effects on Photoelectrochemical Performance of Flexible ZnO Electrodes," *Scientific Reports*, vol. 9, no. 1, p. 11006, 2019.
- 59 Q. Yu *et al.*, "Gas sensing properties of self-assembled ZnO nanotube bundles," *RSC Advances*, vol. 3, no. 37, pp. 16619-16625, 2013.
- 60 M. Raja, N. Muthukumarasamy, D. Velauthapillai, R. Balasundaraprabhu, S. Agilan, and T. S. Senthil, "Studies on bundle like ZnO nanorods for solar cell applications," *Solar Energy*, vol. 106, pp. 129-135, 2014.
- 61 V. Kumar *et al.*, "Effect of annealing on the structural, morphological and photoluminescence properties of ZnO thin films prepared by spin coating," *Journal of Colloid and Interface Science*, vol. 428, pp. 8-15, 2014.
- 62 M. Schumm *et al.*, "Secondary phase segregation in heavily transition metal implanted ZnO," *Journal of Applied Physics*, vol. 105, no. 8, p. 083525, 2009.
- 63 V. Russo, M. Ghidelli, P. Gondoni, C. S. Casari, and A. Li Bassi, "Multi-wavelength Raman scattering of nanostructured Al-doped zinc oxide," *Journal of Applied Physics*, vol. 115, no. 7, p. 073508, 2014.
- 64 R. Zhang, P.-G. Yin, N. Wang, and L. Guo, "Photoluminescence and Raman scattering of ZnO nanorods," *Solid State Sciences*, vol. 11, no. 4, pp. 865-869, 2009.
- 65 R. Cuscó *et al.*, "Temperature Dependence of Raman Scattering in ZnO," *Phys. Rev. B*, vol. 75, 2007.
- 66 P. Jakes and E. Erdem, "Finite size effects in ZnO nanoparticles: An electron paramagnetic resonance (EPR) analysis," *physica status solidi (RRL) – Rapid Research Letters*, vol. 5, no. 2, pp. 56-58, 2011.
- 67 E. Erdem, "Microwave power, temperature, atmospheric and light dependence of intrinsic defects in ZnO nanoparticles: A study of electron paramagnetic resonance (EPR) spectroscopy," *Journal of Alloys and Compounds*, vol. 605, pp. 34-44, 2014.
- 68 E. G. Barbagioanni, R. Reitano, G. Franzò, V. Strano, A. Terrasi, and S. Mirabella, "Radiative mechanism and surface modification of four visible deep level defect states in ZnO nanorods," *Nanoscale*, vol. 8, no. 2, pp. 995-1006, 2016.
- 69 H. Kaftelen, K. Ocakoglu, R. Thomann, S. Tu, S. Weber, and E. Erdem, "EPR and photoluminescence spectroscopy studies on the defect structure of ZnO nanocrystals," *Physical Review B*, vol. 86, no. 1, p. 014113, 2012.
- 70 J. Tauc, R. Grigorovici, and A. Vancu, "Optical Properties and Electronic Structure of Amorphous Germanium," *physica status solidi (b)*, vol. 15, no. 2, pp. 627-637, 1966.

- 71 T. Ruf, S. Repp, J. Urban, R. Thomann, and E. Erdem, "Competing effects between intrinsic and extrinsic defects in pure and Mn-doped ZnO nanocrystals," *Journal of Nanoparticle Research*, vol. 18, no. 5, p. 109, 2016.
- 72 S. K. S. Parashar, B. S. Murty, S. Repp, S. Weber, and E. Erdem, "Investigation of intrinsic defects in core-shell structured ZnO nanocrystals," *Journal of Applied Physics*, vol. 111, pp. 113712-113712-7, 2012.
- 73 G. R. E. S. E. P. B. T. Weber, "Quantitative EPR: A practitioners Guide, ed. ," no. Springer Verlag Wein, 2010.
- 74 S. Repp, S. Weber, and E. Erdem, "Defect Evolution of Nonstoichiometric ZnO Quantum Dots," *The Journal of Physical Chemistry C*, vol. 120, no. 43, pp. 25124-25130, 2016.
- 75 A. Lund, E. Sagstuen, A. Sanderud, and J. Maruani, "Relaxation-Time Determination from Continuous-Microwave Saturation of EPR Spectra," *Radiation Research*, vol. 172, no. 6, pp. 753-760, 8, 2009.